Chaofan Huang
H. Milton Stewart School of Industrial and Systems Engineering,
Georgia Institute of Technology,
Atlanta, GA 30332, USA
email: chaofan.huang@gatech.edu

Sunday Aduloju
Fusion Energy Division,
Oak Ridge National Laboratory,
Oak Ridge, TN 37831, USA
email: adulojusc@ornl.gov

John Fritz
Department of Civil and Environmental Engineering,
University of Tennessee,
Knoxville, TN, 37996, USA
email: mhasan22@vols.utk.edu

V. Roshan Joseph
H. Milton Stewart School of Industrial and Systems Engineering,
Georgia Institute of Technology,
Atlanta, GA 30332, USA
email: roshan@gatech.edu

Mark Messner
Applied Materials Division,
Argonne National Laboratory,
Lemont, IL 60439, USA
email: messner@anl.gov

Timothy Truster[1]
Department of Civil and Environmental Engineering,
University of Tennessee, Knoxville,
Knoxville, TN 37996 USA
email: ttruster@utk.edu

Calibration of RAFM Micro Mechanical Model for Creep using Bayesian Optimization for Functional Output

A Bayesian optimization procedure is presented for calibrating a multi-mechanism micromechanical model for creep to experimental data of F82H steel. Reduced activation ferritic martensitic (RAFM) steels based on Fe(8-9)%Cr are the most promising candidates for some fusion reactor structures. Although there are indications that RAFM steel could be viable for fusion applications at temperatures up to 600 °C, the maximum operating temperature will be determined by the creep properties of the structural material and the breeder material compatibility with the structural material. Due to the relative paucity of available creep data on F82H steel compared to other alloys such as Grade 91 steel, micromechanical models are sought for simulating creep based on relevant deformation mechanisms. As a point of departure, this work recalibrates a model form that was previously proposed for Grade 91 steel to match creep curves for F82H steel. Due to the large number of parameters (9) and cost of the nonlinear simulations, an automated approach for tuning the parameters is pursued using a recently developed Bayesian optimization for functional output (BOFO) framework [1]. Incorporating extensions such as batch sequencing and weighted experimental load cases into BOFO, a reasonably small error between experimental and simulated creep curves at two load levels is achieved in a reasonable number of iterations. Validation with an additional creep curve provides confidence in the fitted parameters obtained from the automated calibration procedure to describe the creep behavior of F82H steel.

Keywords: Model calibration, Crystal plasticity, Bayesian optimization, Microstructural modeling, Generalized chi-square distribution

1 Introduction

The realization of nuclear fusion as a clean alternative energy source requires the design and manufacture of fusion plants that are safe and durable as well as produce minimal radioactive waste. These overarching goals place significant demands on the performance of structural materials and limit material choices. Reduced activation ferritic martensitic (RAFM) steels are the most promising candidates for many fusion reactor structures to facilitate simplified waste management, and F82H steel is one of the most well-studied variants of RAFM steels [2–4]. RAFM steels are also preferred structural materials for fusion/fission applications because they have swelling resistance that outperforms their austenitic counterparts. The determination of the structural integrity of the in-vessel components in the fusion reactor for creep damage using design rules requires the availability of the time-dependent allowable stress intensity, S_t. This material property S_t is calculated from the creep rupture stress, the stress corresponding to onset of tertiary creep, and the stress to cause a 1% creep strain [5]. Unfortunately, these values for evaluating the S_t of F82H steel across a broad range of temperatures and applied stresses are not available because these experiments are very difficult and expensive [6,7].

Traditionally, extrapolating creep data from short term experiments may produce unconservative values since creep deformation mechanisms in ferritic martensitic (FM) steels are dependent on stress level. As an alternative, numerical simulation of creep deformation can be a feasible approach to generate the needed creep data for F82H steel [8]. Earlier creep models [9,10] have been developed based on phenomenological approaches that do not capture microstructure evolution, but recent creep models employ physics-based descriptions that capture glide and climb dislocation mechanisms [11], dislocation density, and precipitate evolution [12] in the microstructure. Crystal plasticity (CP) models, initially limited to describing creep in single crystals [13], have now been extended to capture creep in high temperature polycrystals [14].

Also, the nucleation, growth, and diffusion of cavities within grains and along grain boundaries contribute to creep deformation in FM steels. The present understanding of the distribution and size variation of cavities within prior austenite grains (PAG) and along their grain boundaries [15–19] have helped to develop models for capturing individual cavities along the grain boundaries

[1]Corresponding Author.
Version 1.18, December 11, 2024

[20], void growth along grain boundaries in viscoplastic materials [21], plastic dilatation cavity growth along grain boundaries [22] in 2 dimensional domains.

A smeared-cavity-population physically based model [23,24] was extended by Nassif et al. [25] to capture creep strain effects and stress triaxiality in material points of the grains adjacent the grain boundaries. This model describes the physical and material physics/mechanism such as dislocation climb and glide, diffusion of point defects, grain boundary sliding cavity formation, and growth and coalescence common to FM steels. Initially, Nassif et al. [25] calibrated this model to describe the creep deformation of Grade 91, a widely-used FM steel. Subsequently, the effects of uncertainty in the constitutive model parameters were quantified by Behnam et al. [8]. However, this model can potentially be re-calibrated for F82H steel since it has microstructural features and deformation mechanisms that are similar to Grade 91 steel.

Calibration of a CP model can be formulated as an optimization problem in which the misfit between the CP model and the reference data is minimized. CP models can be challenging to calibrate due to large numbers of parameters, computationally-intensive simulations, and high degree of nonlinearity. Various approaches have been applied to this challenging continuous optimization problem, broadly classified as either local or global optimization methods.

Gradient-based (local) optimization methods have gained significantly popularity and proven to be highly effective over the past decades, particularly with the advancement of automatic differentiation. There have been numerous successful applications of gradient-based optimization in deep learning, computational science, and more recently, the calibration of the CP models [26]. Yet, given the complexity of CP models, the corresponding optimization problem is not convex but rather may possess many local optima. Hence, the effectiveness of gradient-based optimization heavily relies on the initialization and may likely get trapped in a local optimum [27]. Significant domain knowledge is required to find good starting values for the parameters, which is not feasible in most of the cases.

Global optimization techniques, such as evolutionary algorithms, are widely adopted as an alternative tool to handle non-convex optimization with many local optima. They have been successfully applied for parameters calibration in viscoplastic models [28–30] and CP models [31–34]. Although global optimization methods can be more effective at finding global minima, they often require numerous evaluations, e.g., on the order of thousands, of the objective function, which can be computationally expensive if the CP models themselves are costly to evaluate.

To tackle the expensive calibration of the CP models, various researchers [35–37] proposed the use of Bayesian optimization [38–41], the state-of-the-art global optimization approach that can achieve comparable results using significantly fewer evaluations of the objective functions compared to the evolutionary algorithm. The essence of Bayesian optimization is to strategically select the next set of parameters for evaluation by first constructing a surrogate model to learn the response surface of the objective function. However, for the problem of model calibration, the theoretical analysis in [1,42,43] suggests that the standard Bayesian optimization is not the most optimal approach given its least squares objective. Instead, Huang et al. [1] built the surrogate model directly between the input material parameters and the physics model output, and then derived the sequential Bayesian optimization selection criterion for the least squares objective. The effectiveness of the Bayesian optimization for functional output (BOFO) proposed by Huang et al. [1] over standard Bayesian optimization has been demonstrated numerically on the calibration of functional output computer code for a loading scenario of a time-dependent vapor phase infiltration problem. We aim to extend the BOFO method to our problem of interest, namely to identify the material parameters such that the creep strain curve (functional output) from our microstructural CP model would match with the experimental creep strain curve.

The goal of this work is to model creep deformation mechanisms in the grains and grain boundaries of F82H steel using a recently enhanced implementation of 3-dimensional Voce crystal plasticity and smeared-cavity-population type damage models within the MOOSE framework [44]. This implementation incorporates a local Newton solver as a robust implicit time integration scheme for the grain boundary state variables, contrasting with the explicit approach in WARP3D finite element (FE) code [45]. The material parameters of this physically based microstructural model are calibrated to match the experimental creep data for two load levels at 600 °C and validated against a third load level. Although the maximum operating temperature is determined by the creep performance and breeder material compatibility, there are indications that F82H steel could still be viable for fusion applications at temperatures up to 600 °C. The BOFO method proposed specifically for calibrating the functional output computer code in [1] is employed for the parameter identification of our microstructural model, with the initial ranges of the parameters determined from preliminary simulations and from uncertainty quantification of time to minimum creep strain rate for Grade 91 FM steel [8]. Enhancements to BOFO such as batch sequencing are also introduced to improve its effectiveness on this challenging calibration problem.

An outline of the remainder of the paper is as follows. In Section 2, physical comparisons and justifications are made about the microstructure of F82H and Grade 91 steels, and the constitutive model form, the finite element model and the transient solver are described. In Section 3, the ranges of the target material properties are established, the objective function is formalized that effectively weights the discrepancy measures between experimental and simulated creep curves, and post-processing of the FE creep curves onto uniform intervals is discussed. In Section 4, the Bayesian calibration approach is detailed, which starts with the standard Bayesian optimization procedure and then discusses the variant proposed in [1] for the calibration of functional output computer code. In Section 5, the discrepancy measure is evaluated on the output from the MaxPro samples, Bayesian optimization iterations are applied to calibrate the model for the 150 and 180 MPa load levels, and the model is validated by simulating the 160 MPa load level. In Section 6, the features, limitations, impact and future extensions of the Bayesian calibration framework are discussed. Conclusions are drawn in Section 7.

2 Micro-structural Model for Creep in F82H Steel

This section first summarizes the material compositions, microstructural features, and deformation mechanisms common between Grade 91 and F82H steels. The similarity of features motivates the retention of the model form proposed in Nassif et al. [25] that combines grain dislocation creep with grain boundary cavitation models. The next subsection briefly describes the constitutive equations that represent the grain and grain boundary interaction mechanisms of this micro-structural model, the material parameters of which are the target in the calibration study of this work. Subsequently, the simulation of creep boundary value problems using the FE code MOOSE is highlighted along with enhancements to the formulation by Rovinelli et al. [46]. Lastly, simulated creep curves using the calibrated parameters for Grade 91 are shown alongside Grade 91 and F82H experimental data to illustrate the desired level of fit from the BOFO calibration procedure. Further discussion of the model form and its refinements are contained in [25,46].

2.1 Material micro-structural and grain-boundary interaction mechanisms in ferritic martensitic steels.

Ferritic martensitic (FM) steels such as Grade 91 and F82H are composed primarily of iron and secondarily of chromium and have a long history of development due to their creep resistance. RAFM steels are variants of Fe (8-9%Cr) FM steel produced by replacing high activation elements such as Mo and Nb with low activation elements such as W, V and Ta. Concentrations of other elements like Cu, Co, Al, Ni and various impurities are also restricted in the process to limit the

Table 1 Chemical Composition (wt by percent) of 9Cr FM steels and RAFM steels [51,52]

	9Cr FM steels		9Cr RAFM steels		
Element	Grade 91	Grade 92	JFL-1	E97	F82H
C	0.09	0.11	0.1	0.11	0.09
N	0.04	0.05	0.05	0.03	0.01
Cr	8.7	9.3	9	9	7.70
Mn	0.35	0.41	0.45	0.4	0.16
V	0.22	0.16	0.19	0.2	0.16
W	-	1.67	2	1.1	1.95
Ta	-	-	0.07	0.07	0.02
Si	0.29	0.1	<0.1	0.04	0.11

generation of high long-term radioactivity [4]. The Mn concentration in RAFM steel is usually kept high to avoid the formation of delta ferrite. The addition of W increases the creep rupture strength but also increases ductile to brittle transition temperature (DBTT) [47,48]. Tantalum in RAFM steel plays a vital role in lowering DBTT through its effect on prior austenitic grain refinement [49], but higher W and Ta content in RAFM steels could adversely decrease the weldability properties [48,50]. However, addition of Ta helps to restrict the grain growth during normalization and acts as a strong carbide former. Several variants of RAFM steels exist such as Eurofer 97, F82H, ODS and CNAs with variation of W, V and Ta within their material composition. However, F82H steel is one of the most well-studied variants of RAFM steels and has a large database of material properties [6]. The chemical composition of various FM steels, including the F82H steel samples used in the creep experiments reported later in this paper, are listed in Table 1.

These FM steels including Grade 91 and F82H exhibit a complex microstructure within their prior austenite grains (PAG) that forms during the normalizing and tempering processes [53,54]. These microstructural features have length scales varying from approximately 30 µm diameter for the roughly equiaxed PAGs down to the laminar lath structures with a layer width of 0.2 µm, with several martensitic blocks and packets existing at intermediate length scales. The numerical modeling of this study considers explicitly only the PAG highest length scale. Analysis of dislocation density of Grade 91 shows an initial dislocation density on the order of $10^{+13}m^{-2}$ [53], which forms particularly within the dense networks of lath boundaries. Meanwhile, a significant portion of the dislocation density within lath interiors can be easily mobilized during creep loading. Another key feature of FM steels are their carbide and nitride precipitates, in particular the M23C6 (M = Cr-rich) precipitates that cluster along PAG and packet boundaries within Grade 91 [53,54]. These precipitates, with diameters around 100 nm [55], contribute to increased creep strength by stabilizing the material at high temperatures and pinning the dislocation networks. Meanwhile, the MX precipitates (M = Nb/Ta/V, X= C/N) with size usually around 20 nm are more uniformly distributed across the packets and block interiors [25]. Besides developments of these phases, it has been observed that other Laves and Z phases could be formed during service under sustained stress and temperature [56,57].

The substitution between Grade 91 and F82H of the alloying elements Mo and Va with W and Ta does not disrupt the overall appearance and role of these aforementioned microstructural features according to different studies. For example, the existing scanning electron microscopy (SEM) images of RAFM steels [48,58] from a range of compositions and austenitizing temperatures confirm the presence of 10-30 µm diameter PAG and M23C6 precipitates along grain boundaries. Note that the alloying element compositions and austenitizing temperature certainly influence the initial size and coarsening of precipitates [48], the PAG size [58], and lath size [59]. Meanwhile, according to the review of Huang et al. [60], F82H shows slightly higher yet similar creep strength to Grade 91 at 600 °C in contrast to other candidate RAFM steels with lower creep strength. Meanwhile, Tan et al. [52] have noted that the size of the M23C6 precipitates in some batches of F82H could easily coarsen to a size of ≥ 200µm which reduces their effectiveness in pinning the grain boundaries during creep. Also, there can be smaller amounts of MX precipitates (~0.12 vol %) in F82H steel compared to ~0.35 % in Grade 91 steel. This lower density of MX precipitates provides lessened grain boundary pinning and thereby can cause F82H to have lower creep resistance to Grade 91 [52]. Nonetheless, the similarities of microstructural features and mechanical behavior between Grade 91 and F82H motivate the recalibration of the Grade 91 model form Nassif et al. [25] pursued in this work.

In FM steel, during both primary and secondary creep, the primary deformation mechanisms involve dislocation motion and point defect motion. Initially, there is a reduction in mobile dislocations [61] followed by the kinetics of high-density immobilized dislocations being influenced by the processes of climb over precipitates and other recovery mechanisms [55]. This manifests as a power-law relationship between stress and creep rate. Additionally, point defects (vacancies and inclusions) utilize subgrain, block, and packet boundaries as diffusional pathways. In pure metals, the diffusion of point defects at high temperatures and low stress typically results in a linear correlation between stress and creep rate [62,63]. When comparing Grade 91 test data from minimum state creep rates obtained across several experiments and load levels [64–66], a distinct shift in the power-law dependence of strain rate with stress becomes apparent near the 100 MPa load level. These observations are critical for devising numerical models of PAG creep deformation.

Meanwhile, the interacting mechanisms within PAG occur simultaneously with the evolving condition of grain boundaries during progressive creep deformation. A significant mode of creep damage, observed experimentally in metals (including low and high chromium alloy steels), involves the formation and enlargement of cavities along grain boundaries [67,68]. Both new cavity nucleation and growth of existing cavities contribute to creep damage evolution [16,17,69,70]. Additionally, grain boundary sliding has been detected in Grade 91 [16,71], contributing to overall creep strain and creating stress concentrations around particles and triple junctions that drive cavity formation. Consequently, analysis of these features suggests that a physics-based grain boundary model for creep damage should be chosen to consider the intrinsic connections between these processes and the state of neighboring grains.

2.2 Micro-structural creep model: MOOSE code and problem description. Following the discussion on the constitutive relations within the microstructural finite element analysis approach, the focus of this subsection is to briefly describe the history of the numerical implementation of the model within two finite element codes. Then, the spatial and temporal discretization of the F82H unit cell model is described in regards to simulating creep boundary value problems.

In the analysis of the preceding experimental data related to FM steels, two primary mechanisms emerge: (a) the collective deformation of grain bulks, influenced by both dislocation motion and point defect diffusion, and (b) the local deformation of grain boundaries due to viscous sliding as well as void formation, growth, and coalescence. These observations serve as the basis for a micromechanical finite element modeling approach, which considers both grain boundary and bulk deformation using a three-dimensional (3D) cell model. Figure 1 illustrates a typical microstructure, featuring (a) prior austenite grains (PAG) represented as solid elements and (b) prior austenite grain boundaries (PAGB) represented as interface elements. The major constitutive relations which are applicable for representing these two primary microstructural features of FM steels have been developed in our prior work on Grade 91 [25,46]. For completeness, the major relations are provided in Appendices A and B.

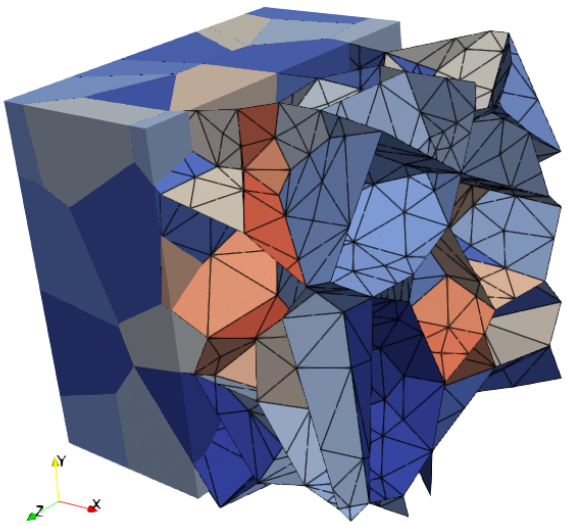

Fig. 1 FE microstructural cell model of F82H, with solid elements representing PAG and interface elements representing PAGB.

The original development and implementation of the Grade 91 microstructural creep model took place in the finite element code WARP3D [45], and its model parameters were manually calibrated to fit the experimental datasets of Kimura et al. [66], and Kloc and Sklenička [64]. However, subsequent work by Rovinelli et al. [46,72] led to the re-implementation of the creep constitutive model form using the MOOSE finite element framework [44]. Specifically, their work is contained within a MOOSE application called DEER (https://github.com/Argonne-National-Laboratory/deer) and will be referenced herein simply as "MOOSE".

The MOOSE implementation offers several enhancements that better suit the automated calibration process for F82H steel; these enhancements are described in greater detail within [72]. Notably, adjusting material parameters introduces a wide range of time scales into the simulated creep curves, spanning three orders of magnitude [8]. To achieve numerical stability across this broad range, the MOOSE platform incorporates a local Newton solver as a robust implicit time integration scheme for the grain boundary state variables, contrasting with the explicit approach in WARP3D. Implicit time integration allows the global FE transient solver to converge efficiently, eliminating the need for meticulously crafted time step sequencing in the WARP3D analyses [25].

Additional enhancements from [72] that also contribute to the numerical robustness of the MOOSE implementation are briefly enumerated:

(1) Smooth Penalty Function for Contact Modeling: Compared to the previous linear penalty function, the relation proposed in (B8) helps reduce the amount of interpenetration.
(2) Adaptive Sub-stepping in Local Newton Solver: The grain boundary quadrature point Newton solver includes adaptive sub-stepping such that failure to converge the state variable evolution equations triggers a local sequential time step calculation rather than triggering a global time step division.
(3) Consistent Algorithmic Tangent Matrix Computation: Because of the adaptive sub-stepping for the grain boundary model, the work of Pérez-Foguet et al. [73] is employed to compute the consistent algorithmic tangent matrix using a formulation of the implicit function theorem.
(4) Enforcing Three Physical Constraints along the Grain Boundaries using Lagrange Multipliers: A void cannot close or shrink below the radius of the carbide particle ($a \geq a_0$); the cavity number density remains non-decreasing ($\dot{b} \leq 0$); and a grain boundary is fully damaged once $b = a$ so that generally $b > a$.
(5) Transitional Near-Failure Model at High Values of Porosity: The grain boundary damage model as a function of porosity $\sqrt{(a/b)}$ exhibits exponential behavior near failure. To mitigate numerical challenges, a smoother traction-separation law that decays to zero is employed once a material point is labeled as "near-failure". This label is determined locally for each grain boundary quadrature point by evaluating three criteria in terms of the local state variables.

Similar to our previous work on Grade 91 steel, the present calibration study on creep behavior of bulk F82H uses a 3D microstructural cell FE model. The FE model includes 100 regions representing prior austenite grains. The polycrystalline mesh generator Neper [74] can create both cuboid and fully periodic grain collections through Voronoi tessellation and space-filling with quadratic tetrahedral elements (as shown in Figure 1). MOOSE creates zero-thickness interface elements using its "BreakMeshByBlockGenerator" command, which employs node duplication procedures from [75]. The cell model used for finite element analysis has dimensions of $0.2 \times 0.2 \times 0.2\text{mm}^3$, resulting in an average grain size of approximately 50 µm with a log-normal distribution and sampled from a random texture. The standard cuboid model consists of 15,494 nodes and 6,159 elements. Notably, Messner et al. [76] demonstrated that using 100 grains adequately reproduces the macroscopic material behavior of Grade 91 when employing block periodic boundary conditions.

In this study, each uniaxial creep simulation adheres to a common load-hold strategy, in which we apply symmetry boundary conditions on the three faces ($x = 0, y = 0, z = 0$), and nodes along the transverse faces ($y = 0.2$ and $z = 0.2$) are constrained to move as a plane in the normal direction. The applied traction on the x-face increases linearly from 0 to the prescribed load level over 0.1 hours and remains constant for the remainder of the simulation. This procedure replicates the triaxial creep test methodology proposed in [77], which accounts for the dead-load imposed on the creep specimen through constant force boundary conditions and mitigates the unit cell free-surface effects. Because the strain rates exhibited by the unit cell are small, the governing equations are considered as quasi-static, and thus the time dependence happens only from the ODE state variable equations which are solved with Backward Euler time integration. Generically, the solution at time t_n serves as the basis for computing the solution at the subsequent time step, $t_{n+1} = t_n + \Delta t$, where Δt represents the time step for that interval.

These creep simulations pose challenges due to their inherent nonlinearity, resulting in stiff nonlinear equations. The computational cost is substantial, with simulation times ranging from 10 to 30 hours when utilizing 10 parallel cores. To address this, we employ adaptive time stepping. Specifically, we adjust the time step Δt to ensure convergence of the nonlinear equation solver. In an adaptive scheme, we target 5 Newton iterations. If 4 or fewer iterations occur in the previous step, we increase Δt, while more than 6 iterations prompts a decrease.

2.3 Calibrated model performance for Grade 91 and experimental creep curves for F82H. Combining together the constitutive model forms with the spatial and temporal representation of the microstructural unit cell, the MOOSE FE code realizes a physics-based model for mapping the applied stress level into the creep strain versus time response of FM steel. We calculate the creep strain as the average engineering strain in the loading direction simulated by the FE model. The unit cell representation herein cannot account for the details of creep crack propagation through

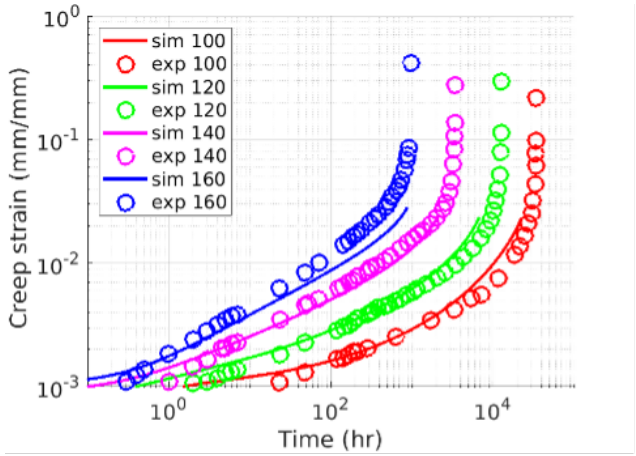

(*a*) Calibrated Grade 91 creep model.

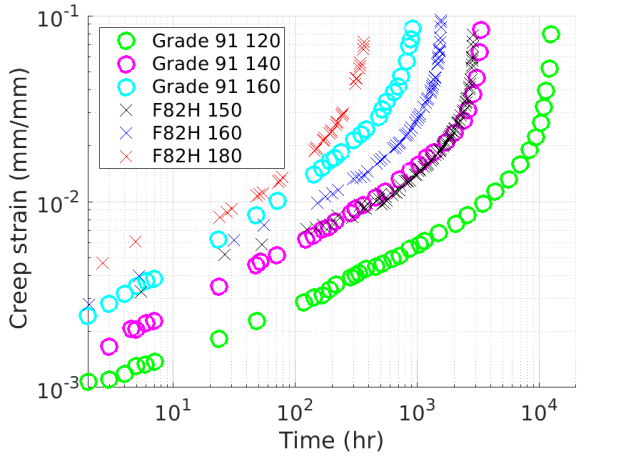

(*b*) Experimental data of Grade 91 and F82H steel.

Fig. 2 Creep curves of FM steels.

a component or sample and so we select a fixed value of strain, specifically 6%, as a consistent termination criteria.

To illustrate the character of FM steel creep curves, we present the log-log representation of the Grade 91 calibrated creep curves in Figure 2(*a*), where the legend reports the applied stress level in MPa. Herein, "creep strain" is reported as engineering strain representing the volume average of the unit cell to match with the relative elongation reported in [51]. The solid lines are the WARP3D FE simulated creep curves [25] and the circles are the experimental data [66]. These curves depict the characteristic behavior of creep, showing strain accumulation over time as a stress-driven process. The simulated creep curves generally capture the trend of the Grade 91 experimental data, although the log-log scale accents the values at earlier elapsed time in contrast to linear-linear plots that accent later-time fitness. Next, in Figure 2(*b*), we compare the experimental creep curves for Grade 91 [66] and F82H [51] at 600 °C across three similar load levels. Notably, F82H appears slightly stronger than Grade 91 at a stress level of 160 MPa since the strain accumulation of F82H occurs over a longer time period than Grade 91. Producing simulated creep curves from the MOOSE code that closely match the data in Figure 2(*b*) is the target for the work of the following sections.

3 Calibration of Crystal Plasticity Models for Creep in F82H Steel

Our goal in this paper is to achieve a comparable level of accuracy in simulating the F82H creep curves as achieved for the calibrated Grade 91 model in Figure 2(*a*). Qualitatively, this goal entails modifying the parameter values in Tables 4 and 5 such that the simulated creep curves from MOOSE at stresses 150, 160, and 180 MPa are close to the experimental F82H creep curves in Figure 2(*b*). A distinguishing feature of the present study is that the material parameters of both volumetric and interfacial governing partial differential equations will be calibrated simultaneously, producing a challenging inverse problem.

In the upcoming parts of this section, we start by firstly establishing the ranges for key material parameters that we will calibrate, then presenting the mathematical model for the calibration problem including motivation of the error metric, and lastly discussing a post-processing step of the MOOSE FE code result for developing datasets for the following analysis and model fitting.

3.1 Key material parameters and their ranges.

By examining Table 4 and Table 5, there are 22 material parameters within the FM steel model form. Of these 22 parameters, 13 are either physical constants, material properties directly measurable from simple experiments, or have been found to have limited sensitivity on the simulated creep curves [8]. These parameters are addressed first, followed by estimating ranges on the remaining 9 parameters.

Beginning first with the PAG parameters, the Young's modulus E and Poisson's ratio ν are assigned using experimental data at 600 °C reported in [3]. The initial slip resistance γ_0 is linked via r through the power law relation to τ_0 and τ_{sat}; thus, its value is retained from the Grade 91 parameter set in Table 4. Lastly, the diffusional creep constant A primarily relates to behavior at lower applied stress level. Since the current calibration is performed for stresses exceeding 100 MPa, the value of A is also retained from [25].

Next considering the PAGB parameters, the traction nucleation exponent β and cavity half tip angle Ψ are commonly adopted values from cavity growth models [24,25]. The interface elasticity parameters (E_{GB}, G_{GB}, W and $P|_{-W}$) have been estimated for numerical stability in [72] and are retained in this study. The normalized maximum cavity density $\frac{N_{\max}}{N_I}$ is linked to the normalized nucleation rate constant $\frac{F_N}{N_I}$ such that the former will be retained from the Grade 91 parameter set in Table 5. Lastly, Behnam et al. [8] found that the initial cavities half radius a_0 is an insensitive parameter for the creep behavior of Grade 91, and thus the value is retained as a value representing typical radii of the M23C6 precipitates in FM steel alloys.

After adjusting the values of these parameters, we arrive at the summarized list of parameters in Table 2 for the F82H creep model. Each of the 9 free parameters are assumed to have a linear variation with the following exceptions: the creep exponent r is restricted to integer values, and D and η_S are assumed to have a logarithmic variation. The mean values of these nine parameters were estimated through manual tuning during initial exploration by the authors launching from the Grade 91 parameter values in Table 4 and Table 5. To determine the parameter ranges, we followed a similar approach employed in [8] for an uncertainty quantification study of Grade 91 steel. Specifically, we considered temperature-dependent material properties related to creep rupture of Grade 91 between 550 °C and 650 °C, as documented in the work by Messner et al. [78]. While the parametric ranges in Table 2 might appear fairly narrow, their variation is still large enough to produce creep curves with several orders of magnitude variation in the time to 6% strain as reported in the later sections of this paper.

3.2 Mathematical model for calibration problem.

Calibration is a type of an inverse problem, i.e., we want to find the input of a model that gives the desired output. Like typical inverse problem formulations involving FE models, we can view the MOOSE code as a black box forward model that maps material parameters (input) into creep curves (output). Mathematically, let $H : \Theta \rightarrow \mathcal{Y}$ denote the MOOSE code, where Θ denotes the calibration space of the nine material parameters and $\mathcal{Y}$ denotes the space of the creep

Table 2 F82H creep model input parameters and their range of variation.

Parameter	Min	Max	Type
E	178000	178000	Fixed
v	0.3	0.3	Fixed
r	12	15	Integer
τ_0	28	52	Linear
τ_{sat}	12	18	Linear
θ_0	800	1000	Linear
$\dot{\gamma}_0$	3.0×10^{-8}	3.0×10^{-8}	Fixed
A	1.2×10^{-9}	1.2×10^{-9}	Fixed
β	2	2	Fixed
n	5	5	Fixed
a_0	5.0×10^{-5}	5.0×10^{-5}	Fixed
b_0	0.06	0.08	Linear
D	2.00×10^{-16}	3.00×10^{-15}	Log
Ψ	75	75	Fixed
Σ_0	200	260	Linear
F_N/N_I	2.00×10^4	2.60×10^4	Linear
$N_{\max}/N_I$	1.0×10^3	1.0×10^3	Fixed
η_S	3.00×10^5	4.00×10^6	Log

curves. The objective of calibration is to find the optimal material parameters $\theta^* \in \Theta$ such that the discrepancy between the MOOSE code output $H(\theta^*)$ and the experimental creep curve $y^* \in \mathcal{Y}$ is minimized, i.e.,

$$\theta^* = \arg\min_{\theta \in \Theta} f(\theta) = \int_x [H(x;\theta) - y^*(x)]^2 dx, \tag{1}$$

where the squared norm is used for measuring the discrepancy. Note that the space of creep curves $\mathcal{Y}$ is a set of square-integrable functions with input x. This is known as the L_2 calibration, and its statistical properties are studied in [79]. The two main reasons for choosing to measure discrepancy via the squared norm (i.e. functional data) as opposed to selected features of the test data are 1) to provide a larger dataset for optimization of the nine material parameters and 2) to better capture all three regimes of the creep process, providing confidence in using the calibrated model in triaxial and other loading scenarios.

Typically the creep curves are defined with abscissa, i.e., x-axis in the coordinate system, representing time and ordinate representing strain (Figure 2). While the shape of the creep curves for each load are similar, the time axis varies by several orders of magnitude. Similarly in [8] and the simulation results herein, some model parameter combinations take 50 hours to reach 6% creep strain value, while some take more than 5000 hours. This variation makes it very difficult to evaluate (1), the squared error between curves measured along the strain axis, as it is not reasonable to estimate a strain value at time 5000 hours if we only observe the simulation creep strain curve to 50 hours. Instead, we see that all the curves are running up to 5% to 6% strain. Hence, contrary to the standard presentation of creep curves, for our calibration approach we will exchange the axes, using strain as the abscissa and time as the ordinate. In another words, let us denote $y^*(x)$ for the duration in the physical experiment taken to attain x% strain value and $H(x;\theta)$ for the corresponding amount of time required by MOOSE code with the material parameter θ. An example of the exchanged figures are shown in Figure 3.

As shown in Figure 2(*b*), we have three available experimental creep curves at 600 °C from [51]: at applied stresses 150, 160, and 180 MPa. We choose to reserve the 160 curve for validation and will use 150 and 180 for calibration to capture a larger loading range. Let $H^{(150)}$ and $H^{(180)}$ denotes the MOOSE code for the 150 and 180 MPa respectively, similarly let $y^{*(150)}$ and $y^{*(180)}$ denotes the flipped experimental creep strains for 150 MPa and 180

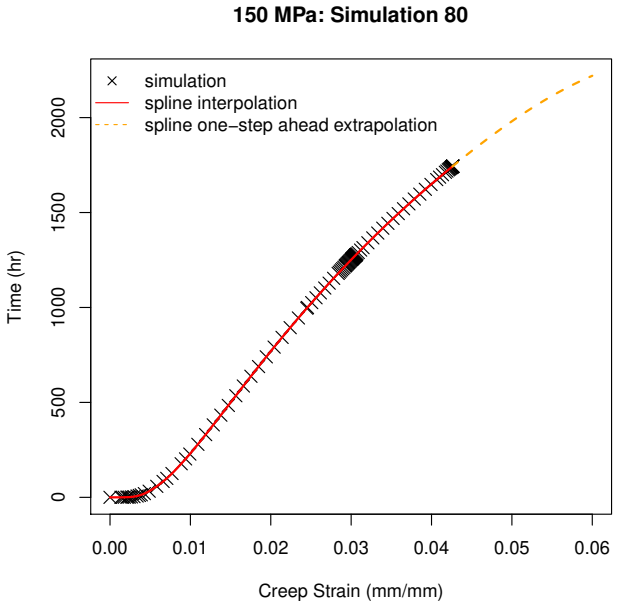

Fig. 3 Simulated creep curves expressed on graphs with exchanged strain and time axes. Post-processing using splines is applied to interpolate and extrapolate the curves at uniform strain intervals between 0% and 6% strain.

MPa. Following these observations, the final objective function for the calibration is

$$\begin{aligned} f(\theta) =& w f^{(150)}(\theta) + f^{(180)}(\theta), \\ f^{(\bullet)}(\theta) =& \int_{0\%}^{6\%} [H^{(\bullet)}(x;\theta) - y^{*(\bullet)}(x)]^2 dx, \end{aligned} \tag{2}$$

where w is some weight that balances the fits between the two experimental data, e.g., picking $w = 1$ considers a simple average between the two squared errors. From Figure 2(*b*), we can see that their values exhibit very different magnitudes: the range is from 0 to 3000 for 150 MPa while for 180 MPa it is only from 0 to only 400. A simple summation would favor finding parameters that better fits the experimental data from 150 MPa. Hence, it is more appropriate to consider

$$w = \frac{\mathrm{Var}(y^{*(180)})}{\mathrm{Var}(y^{*(150)})}, \tag{3}$$

which is the ratio between the variances of the two experimental observations. Hence, the weighted objective function (2) becomes the target for finding θ^* using the BOFO method. The effectiveness of this objective at yielding close fits to both the 150 and 180 MPa creep curves will be assessed in Section 5.

3.3 Post-processing of MOOSE results. Two features of the simulated creep curves from MOOSE emerge from examining Figure 3 that will lead to challenges for computing the objective function (2). Firstly, because creep simulations are load rather than displacement driven as well as because of the adaptive time control, simulations from different material parameters do not record values of elapsed time at the same predefined sequence of accumulated strains. Secondly, the material properties significantly influence the rate at which strain accumulates. In certain cases,

the parameter set introduces a higher degree of nonlinearity or difficulty. Specifically, when the strain level reaches a point where the unit cell becomes significantly distorted, the nonlinear equation solver may fail. Typically, this occurs at strains greater than 6%, although occasionally it may be less as illustrated in Figure 3. Even if the strain reaches 5%, it is still considered a valuable calibrated parameter set that can be accepted. Common reasons for convergence failure include large element distortion, substantial gaps between grains, approaching saturation stress in the crystal plasticity model, difficulties in local extrapolation for the Newton method, and encountering division by zero or fractional powers of negative numbers.

Hence, for the subsequent analysis and model fitting, we first post-process both the simulation and the experimental creep curves to some standardized format. Namely, we want all data to have time values defined on a carefully designed set of creep strain values: $0.0000, 0.0003, 0.006, \ldots, 0.0597, 0.0600$, total of 201 equally spaced points between 0 and 6%. For the case where the simulation reaches 6% creep strain value, we fit a monotonic interpolating spline using Hyman filtering [80] and obtain the time estimation for reaching different creep strain values from the spline directly. Monotonic spline is used because the time it takes to reach a specific strain value always increases as the strain value climbs. For the case that the simulation does not reach 6% creep strain (Figure 3), we need to first extrapolate the time vs. creep strain curve to 6% creep strain value. This is done by first fitting an interpolating spline with the available simulation data, and then performing one-step ahead prediction repeatedly until the creep strain curves reach 6%. The orange dashed line in Figure 3 shows the extrapolation for one of the simulations that did not reach 6% creep strain value. Similarly, we perform the same post-processing step for the experimental data (Figure 2(*b*)) but using smoothing splines [81] to handle the noisy data.

4 Bayesian Optimization for Calibration

Following the description of the calibration problem and mathematical models to solve the problem in Section 3, this section describes the theoretical and numerical aspects of solving this optimization problem with an efficient approach. Recall from Section 3 that the objective is to solve for the material parameters $\theta^* \in \Theta$ such that the simulation creep curves from the MOOSE code match with the experimental ones according to (1). However, the complexity of the MOOSE code H prevents the derivation of analytical gradients and hence hinder the use of first-order optimization methods such as gradient descent. Though numerical gradients could be computed via finite difference method, this approach requires many evaluations of the forward model H, making it practically infeasible given each evaluation takes more than 20 hours. Furthermore, this substantial computational burden also impedes the use of the genetic algorithm, which also typically requires thousands of samples, i.e., thousands evaluations of H. Hence, our goal is to solve (1) using as few evaluations of the forward model H as possible. A Bayesian optimization based solution method named Bayesian Optimization for Functional Output (BOFO) developed in [1] is used to solve this optimization problem. In the following parts of this section, the features of standard BO are first reviewed before highlighting the suitable features of BOFO, a batch sequencing extension of BOFO to accommodate discrete parameters and expensive forward models is discussed, and a flow chart of the algorithm is presented.

4.1 Standard Bayesian optimization. Bayesian optimization (BO) [41] is one of the leading methods for solving optimization problems with expensive objective functions. The standard BO procedure first constructs a probabilistic surrogate model $\hat{f}$ to approximate the response surface of the complicated and multimodal objective function f in (2) and then leverage this predictive information to strategically select the next design via an acquisition function. Expected Improvement (EI) [82] is one popular acquisition function that finds the design which maximizes the improvement over the current optimal in expectation, i.e.,

$$\alpha_{\text{EI}}(\theta) = \mathbb{E}\left[\{f_{\min} - \hat{f}(\theta)\}^+ | \mathcal{D}_n\right], \tag{4}$$

where $\{\bullet\}^+ = \max(\bullet, 0)$ denotes the Macaulay brackets, $\mathcal{D}_n = \{(\theta_i, f(\theta_i)\}_{i=1}^n$ is the set of designs that we have evaluated the objective function up to iteration n, and $f_{\min} = \min_i f(\theta_i)$ is the optimal value from the existing data. The next design is computed from maximizing the acquisition function (4). The BO procedure iterates until a stopping criterion is met, e.g., reaching the budget limit or minimal improvement in the optimal value.

One choice of the surrogate model is the Gaussian process [83, 84], which is specified by a mean function $\mu : \Theta \to \mathbb{R}$ and a covariance function $\mathcal{K} : \mathbb{R}^d \times \mathbb{R}^d \to \mathbb{R}$. Conditional on the existing designs $\mathcal{D}_n$, the predictive distribution of $\hat{f}$ on a new unseen design θ is

$$\hat{f}(\theta)|\mathcal{D}_n \sim \mathcal{N}(\tilde{\mu}(\theta), \tilde{\sigma}^2(\theta)), \tag{5}$$

where

$$\begin{aligned} \tilde{\mu}(\theta) &= \mu(\theta) + \mathcal{K}(\theta, \boldsymbol{\Theta})\mathcal{K}(\boldsymbol{\Theta}, \boldsymbol{\Theta})^{-1}(f(\boldsymbol{\Theta}) - \mu(\boldsymbol{\Theta})), \\ \tilde{\sigma}^2(\theta) &= \mathcal{K}(\theta, \theta) - \mathcal{K}(\theta, \boldsymbol{\Theta})\mathcal{K}(\boldsymbol{\Theta}, \boldsymbol{\Theta})^{-1}\mathcal{K}(\boldsymbol{\Theta}, \theta), \end{aligned} \tag{6}$$

where $\boldsymbol{\Theta} = (\theta_1, \ldots, \theta_n)$. The above can be derived from the property of the conditional multivariate Gaussian distribution. With the Gaussian predictive distribution, the EI acquisition function (4) can be derived in closed-form,

$$\alpha_{\text{EI}}(\theta; \mathcal{D}_n) = \Delta(\theta)\Phi\left(\frac{\Delta(\theta)}{\tilde{\sigma}(\theta)}\right) + \tilde{\sigma}(\theta)\phi\left(\frac{\Delta(\theta)}{\tilde{\sigma}(\theta)}\right), \tag{7}$$

where $\Delta(\theta) = f_{\min} - \tilde{\mu}(\theta)$, and $\Phi(\cdot)$ and $\phi(\cdot)$ are the cumulative distribution function and probability density function of the standard normal distribution, respectively. Maximizing the acquisition function not only favors exploring the high uncertainty region of the response surface but also attempts to locate a better solution, demonstrating the balancing between exploration and exploitation.

Last, an initial design is necessary for the preliminary exploration of the parameter space, for which we utilize the Maximum Projection (MaxPro) designs [85,86]. MaxPro designs is chosen over other popular designs such as Latin Hypercube [87] and Maximin [88] for ensuring a good space-filling property on any subset of the factors, which have been proven to be effective in many real world applications [1].

4.2 Bayesian optimization for calibration of functional output model. However, given the least square objective in (2), the standard BO procedure that builds the surrogate model on f may not be the optimal approach [42,43], since (i) it can only retrieve some aggregated insights about the forward model H and (ii) it cannot guarantee that the prediction from the surrogate model is non-negative. Recently, Huang et al. [1] proposed a BOFO approach specifically designed to address the optimization problem in the form of (2), in which the surrogate model (Gaussian process) is fitted to emulate the complicated forward model H. In this way the full input/output information from H can be utilized for selecting the next design points. The distinctions of BOFO with respect to standard BO are summarized below.

Directly fitting a Gaussian process emulation on the functional output data is known to be computationally very expensive [89,90] due to its high dimensionality. Functional principal component analysis [91] is one efficient way to reduce the dimension of the functional data. Similar to how principal component analysis (PCA) [92] is applied to vectors of data, functional PCA is applied

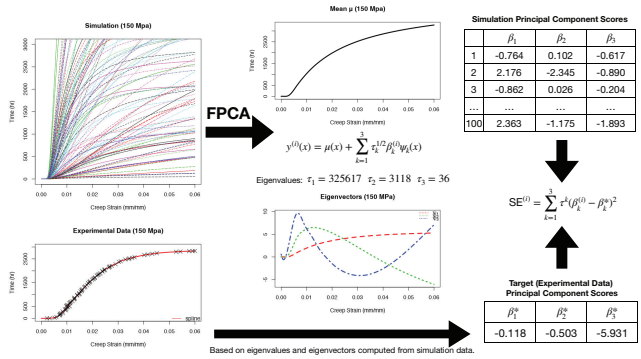

	β_1	β_2	β_3
1	-0.764	0.102	-0.617
2	2.176	-2.345	-0.890
3	-0.862	0.026	-0.204
...	...	...	...
100	2.363	-1.175	-1.893

β_1^*	β_2^*	β_3^*
-0.118	-0.503	-5.931

Fig. 4 Workflow of functional principal component analysis that converts interpolated creep curves into principal component scores.

to decompose any square-integrable function $y(x)$ with $x \in \mathcal{T}$ into a set of orthogonal components such that

$$y(x) = \mu(x) + \sum_{k=1}^{\infty} \tau_k^{1/2} \beta_k \psi_k(x), \tag{8}$$

where $\tau_1 \geq \tau_2 \geq \cdots$ are the eigenvalues, $\psi_1, \psi_2, \ldots$ are the respective orthonormal eigenvectors / eigenfunctions, and β_k is the k-th principal component score. As shown in [1], given that ψ_k's are orthonormal, the squared distance between any two functions $y(x)$ and $y^*(x)$ defined on $0\% \leq x \leq 6\%$ can be simplified to

$$\int_{0\%}^{6\%} [y(x) - y^*(x)]^2 dx = \sum_{k=1}^{\infty} \tau_k (\beta_k - \beta_k^*)^2, \tag{9}$$

where β_k^* is the corresponding k-th principal component score for $y^*(x)$ with respect to eigenvalues τ_k's and eigenvectors ψ_k's. Moreover, in practice it is often the case that the top K components can already explain the majority of the variation, and this will give a good approximation of the above squared error. Hence, the objective function (2) simplifies to

$$\begin{aligned} \tilde{f}(\theta) \approx & w \tilde{f}^{(150)}(\theta) + \tilde{f}^{(180)}(\theta), \\ \tilde{f}^{(\bullet)}(\theta) = & \sum_{k=1}^{K^{(\bullet)}} \tau_k^{(\bullet)} [\beta_k^{(\bullet)}(\theta) - \beta_k^{*(\bullet)}]^2, \end{aligned} \tag{10}$$

where the superscripts in the notations refer to the two experimental load levels of 150 MPa and 180 MPa. See [91] and [1] for more details about functional PCA. Please see Figure 4 for the detailed functional PCA workflow on the 150 MPa data. A similar procedure is also applied for the 180 MPa load level.

To evaluate the objective function (10) on any θ, we only need the estimations for the principal component scores $\beta_k^{(150)}(\theta)$ and $\beta_k^{(180)}(\theta)$, and this can be done by fitting independent one-dimensional output Gaussian processes [83,84] on the principal component scores of the simulation data. This substantially accelerates the fitting of the emulator.

Now it is left to derive the acquisition function for finding the next promising design points. Assume that Gaussian processes have been fitted onto $\beta_k^{(150)}(\theta)$ and $\beta_k^{(180)}(\theta)$, in other words that $\hat{\beta}_k^{(150)}(\theta)|\mathcal{D}_n$ and $\hat{\beta}_k^{(180)}(\theta)|\mathcal{D}_n$ will follow some Gaussian distributions. This assumption then implies that the predictive distribution of $\tilde{f}(\theta)|\mathcal{D}_n$ follows a generalized chi-square distribution. Similarly, Huang et al. [1] derived that the corresponding EI acquisition function is

$$\alpha_{\text{EI}}(\theta; \mathcal{D}_n) = \mathbb{E}[\{f_{\min} - \tilde{f}(\theta)\}^+ | \mathcal{D}_n] = \int_0^{f_{\min}} G_{\chi^2}(s) ds, \tag{11}$$

where G_{χ^2} denotes the cumulative distribution function of the generalized chi-square distribution. Although we do not have the closed-form EI acquisition function as in the standard Bayesian optimization, (11) can be evaluated efficiently via quadrature [93] such that the additional computational overhead is minimal. Please see [1] for the detailed derivation and numerical techniques used for efficient estimation.

We note that almost all BO formulations, including this BOFO approach, are formulated for unconstrained optimization over continuous intervals of parameters as in Table 2. If much larger ranges of the PAG and PAGB constitutive parameters are considered, it can be possible that the nonlinear solvers in the MOOSE code simply won't converge and fail to provide useful data even with the extrapolation scheme shown in Figure 3. The current formulation of BOFO does not handle these infeasible regions or unknown constraints. Future work based on approaches for known [94,95] or unknown [96] constraints could help extend BOFO to address this limitation. However, as shown in Section 5, the initial designs generated from Table 2 did not encounter convergence issues while still producing a large range of output response.

4.3 Batch sequential designs for discrete parameters. The usual Bayesian optimization setting is to generate one new design at a time [82]. Therein, the forward model is evaluated on this new design, the input/output pair is added to the simulation data $\mathcal{D}_n$, and the Gaussian process is fitted to the expanded dataset to find the next design. However, for our calibration problem, the parameter r is a discrete parameter restricted to four different integer values, and we want to get a good learning for each value of r. Thus, we instead generate four new designs each run, with one design for each value of r. On the other hand, generating four designs each time also allows for parallel evaluations of the computationally expensive MOOSE model. Thus, we refer to this extension of BOFO as batch sequencing and will explore its suitability on this problem with one discrete parameter and an expensive forward model.

For simplicity, we follow the constant liar heuristic [97] to generate the batch of four designs. We start with a random r, and find the best design for this r via the acquisition function (11). Now instead of evaluating the forward model H on this new design, we set the prediction to be the mean, and add this "fake" input / output pair to the data for updating the Gaussian process to find the next design. We iterate this procedure till we find all four new designs, with one for each value of r, and then evaluate the forward model on all four designs. The creep curves obtained from the MOOSE model on these designs are then post-processed using the procedure in Section 3.3 and then are augmented into the set of designs $\mathcal{D}_n$ to begin the next iteration $n+1$ of the Bayesian optimization.

4.4 Summary of extended BOFO algorithm. In summary, the sequential workflow shown in Figure 5 consists of performing functional PCA on existing creep curves, refitting with Gaussian processes, maximizing the acquisition function on a batch sequence, and running the MOOSE code in parallel on the four acquired design points. This BOFO framework is iterated until a stopping criterion is met and an optimal parameter design θ^* is achieved. The novel extensions of this framework incorporating batch sequencing and weighted functional output will be applied to calibrate the microstructural cell model parameters in Table 2 to the F82H creep curves in Figure 2(*b*).

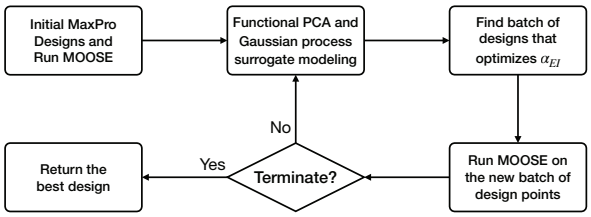

Fig. 5 Workflow of Bayesian calibration of functional output model.

5 Calibration Results

As mentioned in Section 2, in what follows "creep strain" is reported as engineering strain representing the volume average of the unit cell to match with the relative elongation reported in [51]. The creep simulations were performed on a high-performance computing cluster with three nodes having Intel Xeon E5-2687W 3.1 GHz processors with 20 cores and 512 GB memory per node. The simulations were executed by a scheduler that permitted two jobs to run on each node, and the MOOSE code was compiled to use OpenMP shared memory parallelism. The R source code of the BOFO as well as the MOOSE output data and selected input files are available at https://doi.org/10.5281/zenodo.14020513.

5.1 Initial MaxPro design samples. Let us demonstrate the efficiency of the Bayesian optimization method for calibrating the forward model. An initial design of 100 points was employed, which is slightly more than the the popular heuristic $10p$ designs where $p = 9$ is the number of calibrated parameters [98]. The gray circles in Figure 6 are the 100-point initial MaxPro designs generated using the R package `MaxPro` [99]. We can see that the design points are well spread out and cover the calibration region uniformly. As alluded in Section 4.1, the "space-fillingness" is crucial for a comprehensive initial exploration phase of the model, capturing the various input-output characteristics for fitting a good surrogate model.

Figure 7 shows the post-processed MOOSE simulation outputs of the 100-point MaxPro designs. The simulation outputs appear to surround the experimental creep curves, indicating that the chosen calibration range is appropriate. Notice that some simulations indicate a time to 6% strain of 10 hours while others indicate 40,000 hours; thus, even the somewhat narrow range of parameters in Table 2 produces a rather large variation in simulated creep curves. However, it is important to note that despite its coverage, none of the initial design samples provide a satisfactory fit to the experimental data. Therefore, we seek to further refine the calibration via Bayesian optimization.

5.2 Calibration of F82H creep model via Bayesian optimization. Following the workflow in Section 4, the Bayesian optimization is run for 10 iterations with four designs in each iteration, i.e. a total of additional 40 designs on top of the 100 MaxPro designs. The R package `fda` [100] is used for functional principal component analysis, and in all BO iterations the top 3 principal components already explained 99.9% of the variation for both 150 MPa and 180 MPa runs. Thereby, the creep curves from MOOSE are reduced to a 6 dimensional output corresponding to $\beta^{(150)}_{1,2,3}$ and $\beta^{(180)}_{1,2,3}$, and 6 independent Gaussian processes are fitted using the `mlegp` library [101]. The 40 new designs are shown by blue crosses in the Figure 6. We can see that some of them are clustered together, indicating regions of high potential, and some are

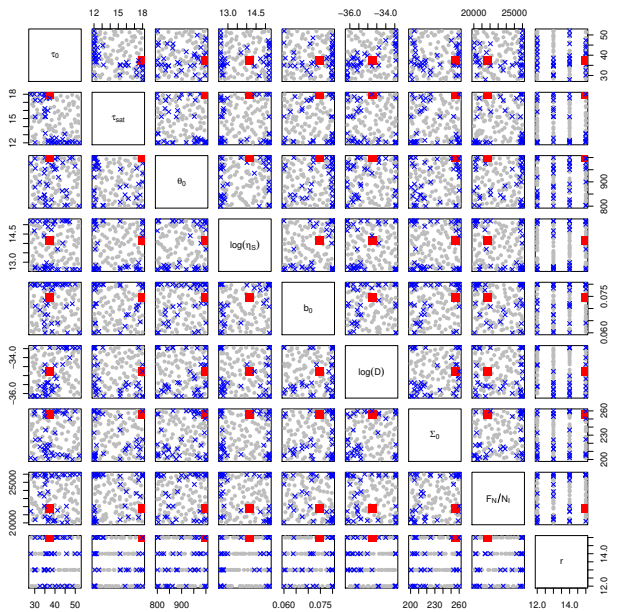

Fig. 6 All parameter designs θ from applying BOFO on the MOOSE code. Gray circles are the initial MaxPro designs; blue crosses are the BOFO sequential designs; and red squares are the best design points θ^*.

far apart from the other, indicating the exploration of uncertainty. This demonstrates the balance between exploration and exploitation in the BOFO approach.

Moreover, Figure 8 shows the value of the objective f versus number of Bayesian optimization iterations, ultimately reaching a objective value that is only one-third of the best objective value obtained from the initial 100-point MaxPro designs. This improvement in fitness is achieved rather effectively by the Bayesian optimization approach in less than half the number of executions of the MOOSE code than in the initial design sampling. The relative cost of the functional PCA and Gaussian process computations to generate the batch of four designs (a few minutes) is much less than that of individual MOOSE simulations (ranging between 100 to 500 adaptive time steps leading to 10 to 25 hours using ten parallel computing threads).

5.3 Evaluation of calibrated parameters and cost of optimization. The values of the parameters θ for F82H steel producing the best design are listed in Table 3 alongside the previous parameter values for Grade 91 steel. Note that other parameters that were not optimized also differ between the two alloys and are listed in Table 2. Also, each of these parameter sets were calibrated to 600 °C creep tests. Overall, the nine parameters appear very similar for Grade 91 and F82H steel, with the largest differences observed in the power-law exponent r and the slip hardening constant θ_0. Returning to the experimental data of the two alloys in Figure 2(*b*), the F82H steel examined in [51] exhibits slightly greater creep resistance at 160 MPa compared to the data in [66]. The calibrated parameters mirror this trend. Namely, the total slip resistance $\tau_0 + \tau_{sat}$ is greater, the diffusion coefficient D is lower, the initial cavity half spacing b_0 is greater, and the traction normalization parameter for cavity nucleation Σ_0 is greater for F82H than for Grade 91, respectively. Each of these parametric variations has previously been found in [76] to result in longer time to 6% strain (higher creep resistance) from the underlying FM steel microstructural model.

Due to the computational cost of the microstructural cell model simulations with MOOSE, alternative calibration approaches were

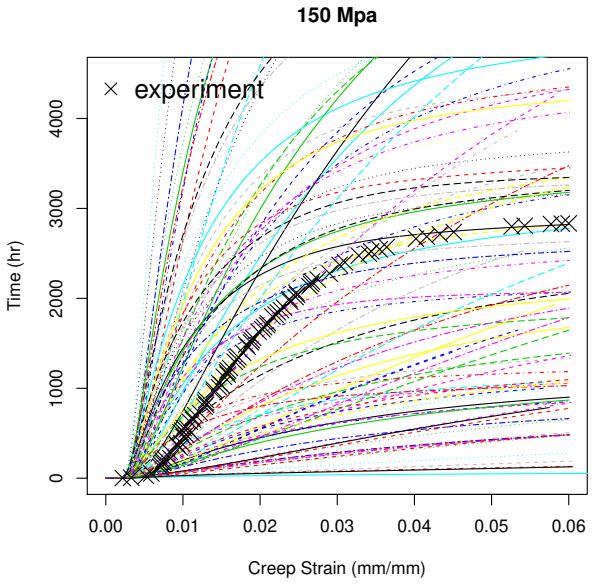

(*a*) 150 MPa.

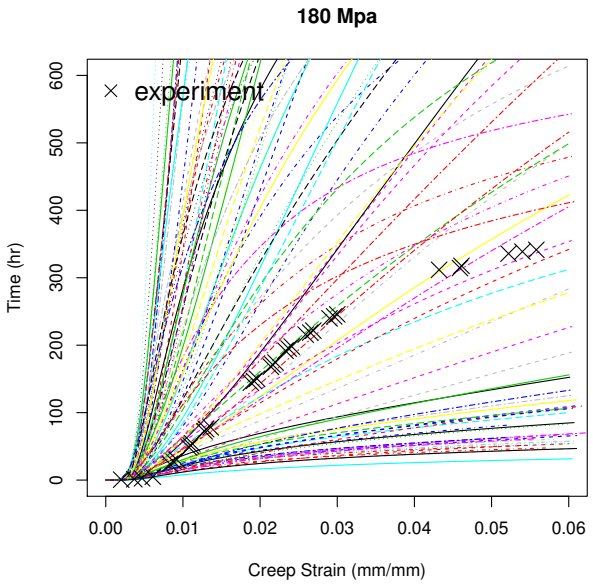

(*b*) 180 MPa.

Fig. 7 Simulated F82H engineering strain vs time curves from initial MaxPro designs.

not performed during this study. However, previous studies on calibration in the literature can place the cost of this Bayesian optimization for functional output (BOFO) in context. Firstly, Huang et al. [1] compared BOFO against other Bayesian optimization approaches for a time dependent partial different equation, and BOFO reduced the root mean square error of the target object by a factor of three with fewer samples than required by other approaches. The amount of reduction in our objective for F82H steel is also a factor of three in Figure 8, and the objective value versus iteration number decays with a similar trend as in [1]. Additionally, three recent Bayesian optimization studies [35–37] have been performed on different crystal plasticity models and loading scenarios. Although the individual runtime of simulations varies between these physical problems and our F82H creep model, the number of forward model evaluations is a typical metric for quantifying the cost of an optimization approach. These models contained between 3 and 5 material parameters, and the total of forward model evaluations (training and testing) was between 100 and 200 to achieve an acceptable fit to experimental data. Meanwhile, the present BOFO approach on the 9-parameter creep model employed 100 initial design points and 10 batches of four evaluations each to achieve an acceptable objective function value. Hence, the present approach exhibited a similar overall cost as the approaches in [35–37] for a problem with more parameters. The batch sequencing extension of BOFO has the added benefit of overlapping runs of the expensive MOOSE code without much hindrance to the decrease of the objective function.

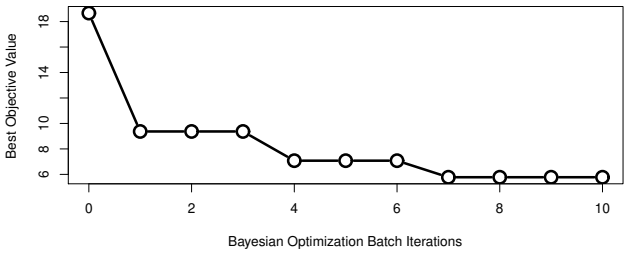

Fig. 8 Best objective value across all current designs versus batch iteration of the Bayesian optimization.

Table 3 The best set of material parameters θ^* for F82H steel compared with the previously calibrated Grade 91 parameters.

Parameter	Grade 91	F82H	Units
r	12	15	Unitless
τ_0	40	37.44	MPa
τ_{sat}	12	17.99	MPa
θ_0	66.67	999.2	MPa
b_0	0.06	0.07465	mm
D	1.0×10^{-15}	7.97×10^{-16}	$\text{MPa}^{-1}\ \text{h}^{-1}\ \text{mm}^3$
Σ_0	200	256	MPa
F_N/N_I	2.00×10^4	2.17×10^4	Unitless
η_S	1.00×10^6	1.40×10^6	$\text{MPa} \cdot \text{h/mm}$

5.4 Validation of calibrated parameters. Finally, Figure 9 compares the experimental data with the simulation results for the best design found through Bayesian optimization. The creep curves at 150 MPa and 180 MPa from this best design appear to capture the trend of the experimental curves quite well. Even on the linear time versus strain plot in Figure 9(*a*), the simulated curves have portions both above and below the experimental curves. Hence, the weighted objective function (10) has provided a balanced fit to both creep curves.

Subsequently for validation, the best design parameters in Table 3 were applied to a FE creep simulation at the 160 MPa load level. The resulting simulated creep curve also appears closely aligned to the 160 MPa experimental curve in Figure 9(*b*). Meanwhile, on the linear time versus strain plot Figure 9(*a*), we observe that the simulation lies slightly below the experimental curve and consequently under-predicts the time to 6% strain. The overall closely aligned 160 MPa validation case demonstrates the generalization capability of the learned design, indicating that it performs well across different experimental conditions, not just the ones it was optimized for. Although not tested, this performance of the underlying physics-based model for F82H steel and the BOFO approach provide confidence that similar results would be reached if

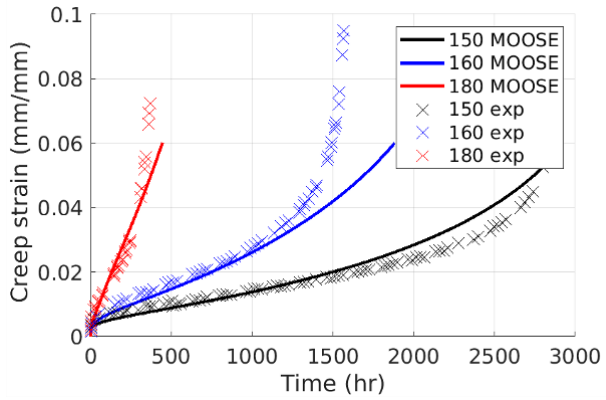

(*a*) Linear scale of strain versus time.

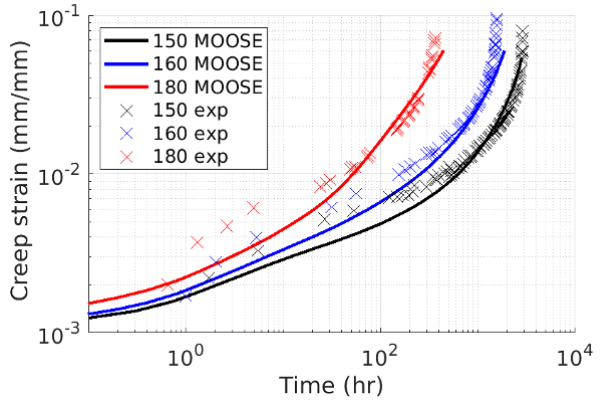

(*b*) Logarithmic scale of strain versus time.

Fig. 9 Calibration and validation of F82H creep model parameters across the 150, 160, and 180 MPa load levels.

either the 150 or 180 MPa load levels were reserved for validation. In summary, with only 140 runs of the forward model, we are able to find a good design that yields simulation output that aligns with the experimental data well.

6 Discussion

6.1 Uncertainty of the calibrated parameters. One drawback of Bayesian optimization is that it can only find deterministic estimates for the calibrated parameters. Yet in many real world applications, understanding the uncertainty of the calibrated parameters is also very important, and Bayesian calibration [102] is widely used to address this. For example, [103,104] have successfully applied Bayesian calibration on CP models, and [105] have applied it on a continuum damage mechanics (CMD) model. However, for a precise estimation of the uncertainty, at least a few thousand samples are required, which is computationally expensive for a CP model that is costly to evaluate. Oftentimes, a surrogate model is generated and the sampling is done using the surrogate model [102,106], but constructing a good surrogate model for a complex microstructural cell model is not easy. Recently, Sürer et al. [107] proposed a new sequential framework to adaptively select the design for building a good surrogate model that can achieve better calibration efficiency.

6.2 Adjusting for missing physics in the F82H creep model. As we can see from Figure 9, even for the best design some parts of the simulated creep curves do not fully capture the shape of the experimental data of F82H steel. This discrepancy indicates there is still some physics about the experimental data that is not

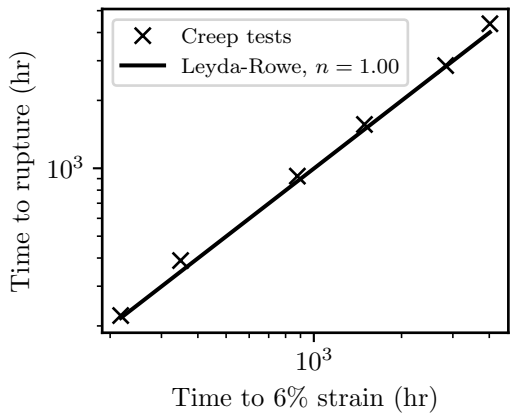

Fig. 10 Plot of the time to 6% strain versus the time to rupture for the available creep data, along with a power-law, Leyda-Rowe model. The Leyda-Rowe model accurately correlates the data for a classical, linear ($n = 1$), relation, meaning we can accurately predict rupture time based on the time to 6% strain.

captured by our microstructural cell model. One approach to account for this missing physics in the calibration process is to apply a statistical adjustment, e.g., using a flexible Gaussian process to account for this discrepancy [102,108]. While this provides enhanced predictability without modifying the underlying PAG and PAGB models, such Gaussian process approaches are a black-box that cannot reveal the structure of the missing physics. Recently, symbolic regression has gained its popularity for discovering physical laws from data [30,109]. Hence, symbolic regression is another promising direction if one is interested in identifying the missing physics in our microstructural modeling based approach for creep in F82H steel.

6.3 Extension for predicting time to rupture. One particular feature in which the simulations deviate from the experimental creep curves is that they underpredict the sharp up-trend in the tertiary creep regime. Prediction of the rupture time, the end of the tertiary regime, is a primary quantity of interest from creep modeling. Three physical factors contribute to tertiary creep:

(1) True softening caused by grain boundary cavitation.
(2) Uniform reduction in cross-sectional area of the specimen under the dead load, leading to an increase in the true stress over time.
(3) Localized deformation leading to necking and a much larger increase in the true stress in the neck.

Of these three factors our model can only capture the first two. The periodic boundary conditions applied in the microstructural unit cell model prevent any localization, meaning we cannot capture necking. For creep ductile materials, like RAFM steels, the large tertiary creep strains occur mostly in the necked region of the specimen. This means our simulations will end — via the development of a smeared crack, represented by the Sham-Needleman model, across an entire plane in the cell model — at strains much lower than those observed experimentally in creep tests. To truly capture the physics of this necking process, some type of multi-scale modeling including the overall component or specimen level response is likely required.

However, our simulations remain physically accurate up to and somewhat beyond the onset of tertiary creep at the minimum creep rate. Predicting the time to the onset of tertiary creep (or time to a fixed strain greater than the strain at the minimum creep rate) is often sufficient to predict the remaining life of the material [110].

More specifically, Figure 10 plots a quasi-Leyda-Rowe relation between the time to 6% strain, our stopping criteria for the simulations, and the time to rupture. The correlation includes data from both the three tests at 600 °C as well as an additional set of tests at 650 °C. The figure demonstrates a clear power law relation between the time to 6% strain and the time to rupture, specifically a classical Leyda-Rowe correlation with a power law exponent nearly equal to 1. By extending the model predictions from the limited strains achievable in the periodic cell domain to the time to rupture through this correlation, our model can reasonably provide a surrogate for the rupture life and strength of the material.

6.4 Impact to the field. The microscale model that is implemented within the MOOSE framework captures the collective deformation of prior austenite grains that is influenced by both dislocation motion and point defect diffusion, and the occurrence of void formation, growth, and coalescence along grain boundaries within the F82H steel. The crystal plasticity parameters within the grains and smeared cavity parameters within the grain boundaries of this model were calibrated and validated at a fusion reactor relevant temperature. The model was found to be provide correct creep strain curves for F82H steel at different stress levels and high temperature. This model provides the capability to predict creep material data such as the minimum or steady state creep rate, minimum stress to cause a 1% creep strain, and minimum stress for onset of tertiary creep at different temperatures and times. It was shown that Leyda-Rowe correlation could help predict the minimum stress corresponding to average creep rupture at various times based on the data generated from this model. These creep material data are important and are needed for determination of the time dependent allowable stress intensities that are required by the structural design criteria for in-vessel components of a fusion reactor. These data that are presently unavailable for F82H steel could be accurately generated from the microscale model that is improved, calibrated and validated in this work. With this contribution, the material database for fusion relevant materials would be enriched and the fusion energy community will be more equipped to determine the structural integrity of the high temperature fusion reactor in-vessel components from the beginning to end of life.

7 Conclusion

This work enhances and applies a recent Bayesian optimization for functional output (BOFO) approach to calibrate the material parameters of a microstructural cell model for creep in F82H steel. This microstructural cell model is based on crystal plasticity and smeared cavity growth models that suitably describe the mechanisms of ferritic-martensitic steels such as Grade 91 and F82H. The implementation of these constitutive models within the MOOSE FE code has been utilized due to its enhanced stability properties for nonlinear problems [72]. Using available creep data for F82H at 600 °C, the calibration problem is posed as minimizing the discrepancy in the squared norm between the experimental and simulated creep curves at 150 and 180 MPa load levels. The ranges for the nine undetermined material parameters in these constitutive models were established utilizing preliminary simulations as well as domain knowledge from studies on Grade 91 [8].

Capitalizing on the form of the weighted squared norm objective function, the BOFO approach of [1] provides advancements over typical Bayesian optimization schemes by constructing a surrogate model directly between material parameters and the creep curves from the MOOSE code, rather than between material parameters and the objective function. This surrogate modeling is made tractable by reducing the dimensionality of the tabulated creep curves into a handful of principal component scores using functional principal component analysis. Launching from the initial design points in the parameter space, the BOFO approach iteratively improves the best-fit material parameters by maximizing the Expected Improvement acquisition function, which balances between exploration and exploitation of the parameter space. The BOFO approach was specialized herein by introducing a batch sequencing based on the constant liar heuristic [97] to generate four design points of material parameters prior to simulation by the MOOSE code. This batch sequencing accounts for the discrete nature of one material parameter r while also enabling concurrent runs of the MOOSE code due to the large computational cost of the creep simulations (100 to 250 CPU hours).

Following the evaluation of the 100-point initial MaxPro designs that cover the parameter space, ten batched iterations of the BOFO approach were performed using the MOOSE code with four runs per iteration and both 150 and 180 MPa load levels in each run. The outcome of the best-fit parameter design for F82H steel in Table 3 was a three-fold reduction in the objective function value from the initial design points. These best-fit parameters were validated by simulating the 160 MPa load level, and the three resulting creep curves showed a strong overall fit to the F82H experimental curves in Figure 9. Thus, 140 total evaluations of the MOOSE code at 150 and 180 MPa load levels were required to calibrate the microstructural cell model for creep in F82H steel, which is a similar number of evaluates exhibited in the calibration of crystal plasticity models using Bayesian optimization [35–37]. A distinguishing feature of the present study is that a relatively larger number of material parameters for both volumetric and interfacial governing partial differential equations were calibrated simultaneously.

The success of this calibration study increases the confidence in the model form developed in [25,72] for describing creep in ferritic-martensitic steels such as Grade 91 and F82H. Although the creep simulations are only performed to recover the time to 6% creep strain, a prediction of the remaining lifetime of the material from these simulations was motivated using a Leyda-Rowe model [110] performed on the limited experimental dataset for F82H at 600 °C and 650 °C [51]. Thus, the batch sequenced BOFO approach was able to produce a validated material parameter set in a reasonable number of forward model evaluations for the challenging calibration problem of the microstructural cell model. This validated creep model for F82H steel has high relevance of the structural design of high temperature fusion reactors by providing a supplement to the presently limited data for creep life of F82H steel.

Acknowledgment

The work of SA and TJT were supported by the Oak Ridge National Laboratory managed by UT-Battelle, LLC for the U.S. Department of Energy (DOE) under contract number DEAC05-00OR22725. The U.S. government retains and the publisher, by accepting the paper for publication, acknowledges that the U.S. government retains a nonexclusive, paid-up, irrevocable, worldwide license to publish or reproduce the published form of this manuscript, or allow others to do so, for U.S. government purposes. DOE will provide public access to these results of federally sponsored research in accordance with the DOE Public Access Plan (http://energy.gov/downloads/doe-public-access-plan).

The work of MCM was sponsored by the U.S. Department of Energy, under Contract No. DEAC02-06CH11357 with Argonne National Laboratory, managed and operated by UChicago Argonne LLC. The work of CH and VRJ were supported by NSF grant DMREF-1921873. The work of JF and TJT were supported by NSF grant CMMI-1751591.

Data Availability Statement

The data and information that support the findings of this article are freely available at: https://doi.org/10.5281/zenodo.14020513.

Appendix A: Prior austenite grain model form

In our microstructural evolution cell model for Grade 91 steel adapted for F82H, the PAG are represented by groups of solid

Table 4 Grain material parameters for Grade 91 at 600 °C

Sym.	Description	Value	Units
E	Young's modulus	150×10^3	MPa
υ	Poisson's ratio	0.285	Unitless
r	Voce hardening exponent	12	Unitless
τ_0	Initial slip resistance	40	MPa
τ_{sat}	Saturation slip resistance	12	MPa
θ_0	Slip hardening constant	66.67	MPa
$\dot{\gamma}_0$	Prefactor	9.55×10^{-8}	h^{-1}
A	Diffusional creep constant	1.2×10^{-9}	$MPa^{-1}\ h^{-1}$

elements with initially identical Euler angles specifying the orientation of the body-centered cubic (BCC) crystal structure. The crystal plasticity formulation employs finite strain kinematics and an additive decomposition of the strain rates for each mechanism by assuming the elastic stretch and rate of elastic stretch remain small. The mechanisms of dislocation creep and diffusional creep are postulated to operate concurrently via the movement of distinct defect types (dislocations and atoms/vacancies). Consequently, the strain rates resulting from each mechanism are aggregated into the total rotated inelastic strain rate $\mathbf{d}^{(i)}$:

$$\mathbf{d}^{(i)} = \bar{\mathbf{d}}^{(p)} + \mathbf{d}^{(d)}, \tag{A1}$$

where $\bar{\mathbf{d}}^{(p)}$ is the crystal plasticity strain rate and and $\mathbf{d}^{(d)}$ is the diffusional strain rate.

Within the temperature and applied stress regime of interest, FM steels primarily exhibit a mechanism involving alternating climb and glide of dislocations over various barriers along preferred crystallographic planes and directions. Power-law dependence between the steady state stress and strain rate in creep tests are characteristic of this glide-climb mechanism, with a larger exponent to account for prevalence of precipitates. Also, experimental creep curves for both Grade 91 [64] and F82H [51] reveal a prolonged period of primary creep attributed to the large dislocation densities and local residual stress variations arising during normalization [25]. Thus, an isotropic Voce hardening model is incorporated within the crystal plasticity constitutive equations for $\bar{\mathbf{d}}^{(p)}$ that follow.

$$\bar{\mathbf{d}}^{(p)} = \sum_{s=1}^{n_{\text{slip}}} \dot{\gamma}^{(s)} \text{sym}(\tilde{\mathbf{m}}^{(s)} \otimes \tilde{\mathbf{n}}^{(s)}) \tag{A2}$$

$$\dot{\gamma}^{(s)} = \dot{\gamma}_0 \left| \frac{\tau^{(s)}}{\tau_0 + \tau_w} \right|^{r-1} \frac{\tau^{(s)}}{\tau_0 + \tau_w} \tag{A3}$$

$$\dot{\tau}_w = \theta_0 \left(1 - \frac{\tau_w}{\tau_{sat}}\right) \sum_{s=1}^{n_{\text{slip}}} \left|\dot{\gamma}^{(s)}\right| \tag{A4}$$

Here, $\dot{\gamma}^{(s)}$ is the slip rate and $\tilde{\mathbf{m}}^{(s)}$ and $\tilde{\mathbf{n}}^{(s)}$ are the slip direction and slip plane normal unit vectors for system (s) within the set of 12 primary $\{110\}\langle\bar{1}11\rangle$ BCC slip systems. The slip rate is mediated by the resolved shear stress $\tau^{(s)}$, the initial drag stress τ_0, the strengthening resistance τ_w, the reference strain rate $\dot{\gamma}_0$, and the exponent r. The strengthening resistance evolves from zero up to a saturation stress τ_{sat} with an initial flow modulus θ_0. The pre-calibrated values of these parameters for Grade 91 [25] are provided in Table 4. In particular, the disparate values of hardening arising from anisotropic dislocation creep in grains of different orientation help induce stress concentrations along grain boundaries that increase the spatial variation of cavity growth in comparison to an isotropic plasticity model [76].

Next, the diffusional creep term is used to account for the linear relationship between the steady-state creep rate and applied stress observed at lower loads. The deviatoric stress serves as a measure of the cell-averaged deformation rate resulting from atomic/vacancy diffusion along various pathways within the complex microstructure of Grade 91. Hence, $\mathbf{d}^{(d)}$ is taken to be directly proportional to the deviatoric stress $\mathbf{s}$ through a self-diffusion coefficient A:

$$\mathbf{d}^{(d)} = A\mathbf{s}. \tag{A5}$$

Appendix B: Prior austenite grain boundary model form

The second major source of creep deformation in FM steels is the relative motion of PAGBs, composed of both in-plane sliding and out-of-plane opening mechanisms. A smeared representation of the formation, growth, and coalescence of a population of cavities is captured in the microstructural model using zero-thickness two-dimensional (2D) interface elements along the boundaries of three-dimensional PAGs. These elements are depicted in Figure 1 and are associated with a traction-separation (cohesive) model. This grain boundary cavitation model is rooted in research by Sham and Needleman [23] on stress triaxiality effects on void growth that was later extended by Van der Giessen and coworkers [24], to account for higher triaxiality values as well as cavity nucleation. Our prior work [25] augmented these cavity growth mechanisms with contributions arising from grain boundary sliding, taking inspiration from studies by Ashby and colleagues [111]. More recently, [46,72] extended this cohesive model from a purely viscous form to a visco-elastic form and improved the numerical stability of the model for nearly-fully-cavitated grain boundaries.

The grain boundary cavitation model is cast into a Maxwell model form consisting of five primary variables: the average cavity half-radius a, the number of cavities per unit area r, the normal traction T_N, and the two shear tractions T_{S_1} and T_{S_2}. The number of cavities per unit area is geometrically related to the average cavity half-spacing b by $b = 1/\sqrt{\pi N}$, and the damaged area fraction of the grain boundary is quantified through the porosity as $(a/b)^2 \leq 1$. The rate equations describing the evolution of each primary state variable are as follows:

$$\dot{a} = \frac{\dot{V}}{4\pi h(\psi) a^2}, \quad F_{\dot{b}} = (\{T_N\}^+/\Sigma_0)^\beta (F_N/N_I), \tag{B1}$$

$$\dot{b} = \begin{cases} -(b^3/b_0^2) F_{\dot{b}} \dot{\epsilon}^C_{eq} & \text{after } F_{\dot{b}} \int_0^t |\dot{\epsilon}^C_{eq}| d\tau \geq 1 \\ 0 & \text{otherwise} \end{cases}, \tag{B2}$$

$$\dot{T}_N = C_N \left([\![\dot{u}]\!]_N + \frac{\dot{V}}{\pi b^2} \right), \tag{B3}$$

$$\dot{T}_{S_{1,2}} = C_S \left([\![\dot{u}]\!]_{S_{1,2}} + \frac{T_{S_{1,2}}}{\eta_S f_S} \right), \tag{B4}$$

where β, n, a_0, b_0, D, ψ, Σ_0, F_N/N_I, and $N_{\max}/N_I$ are model parameters that are named within Table 5. The cavity volume rate $\dot{V}$ influences both a and T_N, and it is described after the other terms below. The cavity nucleation model is driven by the opening traction T_N and local creep deformation rate $\dot{\epsilon}^C_{eq} = \sqrt{\frac{2}{3}\mathbf{d}^{(i)} : \mathbf{d}^{(i)}}$ once sufficient plasticity has accumulated in the neighboring grains. Both the interface normal elastic stiffness C_N and the interface transverse elastic stiffness C_S as well as the degradation function f_S for the grain boundary viscosity are reduced as the porosity increases according to the following relations:

$$C_N = \left(1 - \frac{a}{b}\right) \frac{E_{GB} P([\![u]\!]_N)}{W}, \tag{B5}$$

$$C_S = \left(1 - \frac{a}{b}\right) \frac{G_{GB}}{W}, \tag{B6}$$

$$f_S = \begin{cases} 1 & \text{if } \frac{a}{b} \leq 0.5 \\ 2\left(-\frac{a}{b} + 1\right) & \text{if } \frac{a}{b} > 0.5 \end{cases}, \tag{B7}$$

where E_{GB}, G_{GB}, and W are the grain boundary elastic properties and initial thickness that are also listed within Table 5. An additional interpenetration penalty factor $P(\llbracket u \rrbracket_N)$ is provided to reduce the amount of interpenetration on grain boundaries experiencing compressive traction. Both step-wise discontinuous and quadratic penalty functions were evaluated within [46,72], and the quadratic form provided better numerical stability while still sufficiently reducing the interpenetration for contact along the grain boundaries. This quadratic relation listed below amplifies the normal elastic under compression with a relative amplitude controlled by P_{-W}.

$$P(\xi) = \begin{cases} 1 & \text{if } \xi \geq 0 \\ 1 + (P_{-W} - 1)(\xi/W)^2 & \text{if } \xi < 0 \end{cases} \tag{B8}$$

Finally, the cavity volume rate $\dot{V}$ is composed of two mechanisms. Firstly, void diffusion is accounted for via $\dot{V}^D$ in terms of the opening traction and the grain boundary diffusivity. Secondly, the stress triaxiality effect is represented by $\dot{V}^{triax}$ and is driven by the hydrostatic stress σ_H, the von Mises stress σ_{VM}, and the creep rate $\dot{\epsilon}^C_{eq}$ in the material adjacent to the grain boundary.

$$\dot{V} = \dot{V}^D + \dot{V}^{triax} = 8\pi D \frac{\{T_N\}^+}{q(f)} + \dot{V}^{triax} \tag{B9}$$

$$\dot{V}^{triax} = \begin{cases} F_{a\epsilon} m \left\{\alpha_n \left|\frac{\sigma_H}{\sigma_{VM}}\right| + \beta_n(m)\right\}^n & \text{if } \left|\frac{\sigma_H}{\sigma_{VM}}\right| \geq 1 \\ F_{a\epsilon} \{\alpha_n + \beta_n(m)\}^n \frac{\sigma_H}{\sigma_{VM}} & \text{if } \left|\frac{\sigma_H}{\sigma_{VM}}\right| < 1 \end{cases} \tag{B10}$$

$$f = \max\left(\frac{a^2}{(a + 1.5L)^2}, \frac{a^2}{b^2}\right), \quad m = \text{sgn}(\sigma_H) \tag{B11}$$

$$L = \left(\frac{D\sigma_{VM}}{\dot{\epsilon}^C_{eq}}\right)^{1/3}, \quad F_{a\epsilon} = 2\dot{\epsilon}^C_{eq} a^3 \pi h(\psi) \tag{B12}$$

$$q(f) = -2\ln f - (1 - f)(3 - f) \tag{B13}$$

$$h(\psi) = \left(\frac{1}{1 + \cos\psi} - \frac{\cos\psi}{2}\right) \frac{1}{\sin\psi} \tag{B14}$$

$$\alpha_n = 3/(2n), \quad \beta_n(m) = (n - 1)[n + g(m)]/n^2 \tag{B15}$$

$$g(1) = 0.4319, \quad g(0) = 0, \quad g(-1) = 0.4031 \tag{B16}$$

The parameters from the cavity volume rate equations and the other preceding parameters of the grain boundary cavitation model are collected in Table 5 along with their calibrated values for Grade 91.

Table 5 Grain boundary cavitation material parameters

Sym.	Description	Value	Units
β	Traction nucleation exponent	2	Unitless
n	Creep rate exponent	5	Unitless
a_0	Initial cavities half radius	5×10^{-5}	mm
b_0	Initial cavities half spacing	0.06	mm
D	Grain boundary diffusion coefficient	1×10^{-15}	MPa^{-1} h^{-1} mm^3
Ψ	Cavity half tip angle	75	∘
Σ_0	Traction normalization parameter	200	MPa
$\frac{F_N}{N_I}$	Normalized nucleation rate constant	2×10^4	Unitless
$\frac{N_{\max}}{N_I}$	Normalized maximum cavity density	1×10^3	Unitless
E_{GB}	Interface Young modulus	1.5×10^5	MPa
G_{GB}	Interface in-plane Shear modulus	5.9×10^4	MPa
η_S	Sliding viscosity	1×10^6	MPa · h/mm
W	Interface thickness	0.011	mm
$P\|_{-W}$	Penalty at $\llbracket u \rrbracket_N = -W$	10	Unitless

References

[1] Huang, C., Ren, Y., McGuinness, E. K., Losego, M. D., Lively, R. P., and Joseph, V. R., 2021, "Bayesian optimization of functional output in inverse problems," Optimization and Engineering, **22**, pp. 2553–2574.

[2] Hirose, T., Kato, T., Sakasegawa, H., Tanigawa, H., and Nozawa, T., 2020, "Evaluation of fatigue properties of reduced activation ferritic/martensitic steel, F82H for development of design criteria," Fusion Engineering and Design, **160**, p. 111823.

[3] Aduloju, S. C., Kessel, C., Youchison, D., Rasheed, F., and Nogradi Jr, P., 2022, "Steady state thermo-mechanics and material property definition framework for analyzing DCLL blanket in the fusion nuclear science facility," Fusion Engineering and Design, **183**, p. 113257.

[4] Bhattacharya, A., Levine, S. M., Zinkle, S. J., Chen, W.-Y., Baldo, P., Parish, C. M., and Edmondson, P. D., 2022, "Radiation induced amorphization of carbides in additively manufactured and conventional ferritic-martensitic steels: In-situ experiments on extraction replicas," Journal of Nuclear Materials, **563**, p. 153646.

[5] Sannazzaro, G., Barabash, V., Kang, S., Fernandez, E., Kalinin, G., Obushev, A., Martínez, V., Vázquez, I., Fernández, F., and Guirao, J., 2013, "Development of design criteria for ITER in-vessel components," Fusion Engineering and Design, **88**(9-10), pp. 2138–2141.

[6] Nozawa, T., Tanigawa, H., Kojima, T., Itoh, T., Hiyoshi, N., Ohata, M., Kato, T., Ando, M., Nakajima, M., Hirose, T., et al., 2021, "The status of the Japanese material properties handbook and the challenge to facilitate structural design criteria for DEMO in-vessel components," Nuclear Fusion, **61**(11), p. 116054.

[7] Aduloju, S. C. and Kessel, C., 2024, "Assessment of thermal and radiation induced creep in the dual cooled lead lithium blanket," Fusion Engineering and Design, **201**, p. 114256.

[8] Behnam, A., Truster, T. J., Tipireddy, R., Messner, M. C., and Gupta, V., 2022, "Uncertainty Quantification Framework for Predicting Material Response with Large Number of Parameters: Application to Creep Prediction in Ferritic-Martensitic Steels Using Combined Crystal Plasticity and Grain Boundary Models," Integrating Materials and Manufacturing Innovation, **11**(4), pp. 516–531.

[9] Chaboche, J.-L., 1989, "Constitutive equations for cyclic plasticity and cyclic viscoplasticity," International journal of plasticity, **5**(3), pp. 247–302.

[10] Moosbrugger, J., 1992, "Nonisothermal constitutive model for the small strain behavior of 9Cr-1 Mo-V-Nb pressure vessel steel," Journal of Engineering Materials and Technology.

[11] Dyson, B., 2009, "Microstructure based creep constitutive model for precipitation strengthened alloys: theory and application," Materials science and technology, **25**(2), pp. 213–220.

[12] Christopher, J. and Choudhary, B., 2019, "Prediction of long-term creep behaviour of Grade 91 steel at 873 K in the framework of microstructure-based creep damage mechanics approach," International Journal of Damage Mechanics, **28**(6), pp. 877–895.

[13] Ma, A., Dye, D., and Reed, R., 2008, "A model for the creep deformation behaviour of single-crystal superalloy CMSX-4," Acta Materialia, **56**(8), pp. 1657–1670.

[14] Zhao, J., Gong, J., Saboo, A., Dunand, D. C., and Olson, G. B., 2018, "Dislocation-based modeling of long-term creep behaviors of Grade 91 steels," Acta Materialia, **149**, pp. 19–28.

[15] Wu, R. and Sandström, R., 1996, "Strain dependence of creep cavity nucleation in low alloy and 12% Cr steels," Materials Science and Technology, **12**(5), pp. 405–415.

[16] Gaffard, V., 2004, "Experimental study and modelling of high temperature creep flow and damage behaviour of 9Cr1Mo-NbV steel weldments," Ecole Nationale Superieure des Mines.

[17] Gupta, C., Toda, H., Schlacher, C., Adachi, Y., Mayr, P., Sommitsch, C., Uesugi, K., Suzuki, Y., Takeuchi, A., and Kobayashi, M., 2013, "Study of creep cavitation behavior in tempered martensitic steel using synchrotron microtomography and serial sectioning techniques," Materials Science and Engineering: A, **564**, pp. 525–538.

[18] Shrestha, T., Basirat, M., Charit, I., Potirniche, G. P., and Rink, K. K., 2013,

"Creep rupture behavior of Grade 91 steel," Materials Science and Engineering: A, **565**, pp. 382–391.
[19] Wang, X., Wang, X., Luo, B., and Guo, J., 2018, "Analysis of cavity evolution in 9% Cr heat-resistant steel welded joint during creep," Engineering Fracture Mechanics, **202**, pp. 394–404.
[20] Westwood, C., Pan, J., and Crocombe, A., 2004, "Nucleation, growth and coalescence of multiple cavities at a grain-boundary," European Journal of Mechanics-A/Solids, **23**(4), pp. 579–597.
[21] Rice, J. R. and Tracey, D. M., 1969, "On the ductile enlargement of voids in triaxial stress fields," Journal of the Mechanics and Physics of Solids, **17**(3), pp. 201–217.
[22] Gurson, A. L., 1977, "Continuum theory of ductile rupture by void nucleation and growth: Part I—Yield criteria and flow rules for porous ductile media," Journal of Engineering Materials and Technology.
[23] Sham, T.-L. and Needleman, A., 1983, "Effects of triaxial stressing on creep cavitation of grain boundaries," Acta Metallurgica, **31**(6), pp. 919–926.
[24] Van Der Giessen, E., Van der Burg, M., Needleman, A., and Tvergaard, V., 1995, "Void growth due to creep and grain boundary diffusion at high triaxialities," Journal of the Mechanics and Physics of Solids, **43**(1), pp. 123–165.
[25] Nassif, O., Truster, T. J., Ma, R., Cochran, K. B., Parks, D. M., Messner, M. C., and Sham, T., 2019, "Combined crystal plasticity and grain boundary modeling of creep in ferritic-martensitic steels: I. Theory and implementation," Modelling and Simulation in Materials Science and Engineering, **27**(7), p. 075009.
[26] Chen, T. and Messner, M. C., 2023, "Training material models using gradient descent algorithms," International Journal of Plasticity, **165**, p. 103605.
[27] Li, B., Lin, J., and Yao, X., 2002, "A novel evolutionary algorithm for determining unified creep damage constitutive equations," International Journal of Mechanical Sciences, **44**(5), pp. 987–1002.
[28] Abdul-Hameed, H., Messager, T., Zaïri, F., and Naït-Abdelaziz, M., 2014, "Large-strain viscoelastic–viscoplastic constitutive modeling of semi-crystalline polymers and model identification by deterministic/evolutionary approach," Computational Materials Science, **90**, pp. 241–252.
[29] Yao, D., Duan, Y.-c., Li, M.-y., and Guan, Y.-p., 2021, "Hybrid identification method of coupled viscoplastic-damage constitutive parameters based on BP neural network and genetic algorithm," Engineering Fracture Mechanics, **257**, p. 108027.
[30] Kronberger, G., Kabliman, E., Kronsteiner, J., and Kommenda, M., 2022, "Extending a physics-based constitutive model using genetic programming," Applications in Engineering Science, **9**, p. 100080.
[31] Steglich, D., Brocks, W., Bohlen, J., and Barlat, F., 2011, "Modelling direction-dependent hardening in magnesium sheet forming simulations," International Journal of Material Forming, **4**, pp. 243–253.
[32] Yan, S., Yang, H., Li, H., and Yao, X., 2016, "A unified model for coupling constitutive behavior and micro-defects evolution of aluminum alloys under high-strain-rate deformation," International Journal of Plasticity, **85**, pp. 203–229.
[33] Sedighiani, K., Diehl, M., Traka, K., Roters, F., Sietsma, J., and Raabe, D., 2020, "An efficient and robust approach to determine material parameters of crystal plasticity constitutive laws from macro-scale stress–strain curves," International Journal of Plasticity, **134**, p. 102779.
[34] Savage, D. J., Feng, Z., and Knezevic, M., 2021, "Identification of crystal plasticity model parameters by multi-objective optimization integrating microstructural evolution and mechanical data," Computer Methods in Applied Mechanics and Engineering, **379**, p. 113747.
[35] Nguyen, T., Francom, D. C., Luscher, D. J., and Wilkerson, J., 2021, "Bayesian calibration of a physics-based crystal plasticity and damage model," Journal of the Mechanics and Physics of Solids, **149**, p. 104284.
[36] Kuhn, J., Spitz, J., Sonnweber-Ribic, P., Schneider, M., and Böhlke, T., 2021, "Identifying material parameters in crystal plasticity by Bayesian optimization," Optimization and Engineering, pp. 1–35.
[37] Tran, A. and Lim, H., 2023, "An asynchronous parallel high-throughput model calibration framework for crystal plasticity finite element constitutive models," Computational Mechanics, **72**(3), pp. 485–498.
[38] Kushner, H. J., 1964, "A New Method of Locating the Maximum Point of an Arbitrary Multipeak Curve in the Presence of Noise," Journal of Basic Engineering, **86**(1), pp. 97–106.
[39] Mockus, J., 1994, "Application of Bayesian approach to numerical methods of global and stochastic optimization," Journal of Global Optimization, **4**, pp. 347–365.
[40] Jones, D. R., 2001, "A taxonomy of global optimization methods based on response surfaces," Journal of global optimization, **21**, pp. 345–383.
[41] Frazier, P. I., 2018, "A tutorial on Bayesian optimization," arXiv preprint arXiv:1807.02811.
[42] Uhrenholt, A. K. and Jensen, B. S., 2019, "Efficient Bayesian optimization for target vector estimation," *The 22nd International Conference on Artificial Intelligence and Statistics*, PMLR, pp. 2661–2670.
[43] Matsui, K., Kusakawa, S., Ando, K., Kutsukake, K., Ujihara, T., and Takeuchi, I., 2019, "Bayesian active learning for structured output design," arXiv preprint arXiv:1911.03671.
[44] Giudicelli, G., Lindsay, A., Harbour, L., Icenhour, C., Li, M., Hansel, J. E., German, P., Behne, P., Marin, O., Stogner, R. H., et al., 2024, "3.0-MOOSE: Enabling massively parallel multiphysics simulations," SoftwareX, **26**, p. 101690.
[45] Dodds, R., 2024, "WARP3D User-Theory Manual," http://www.warp3d.net/
[46] Rovinelli, A., Messner, M. C., Parks, D. M., and Sham, T.-L., 2021, "Accurate effective stress measures: predicting creep life for 3D stresses using 2D and 1D creep rupture simulations and data," Integrating Materials and Manufacturing Innovation, **10**, pp. 627–643.
[47] Abe, F., Noda, T., Araki, H., and Nakazawa, S., 1991, "Alloy composition selection for improving strength and toughness of reduced activation 9Cr-W steels," Journal of nuclear materials, **179**, pp. 663–666.
[48] Shankar, V., Mariappan, K., Sandhya, R., Laha, K., Jayakumar, T., and Kumar, E. R., 2015, "Effect of W and Ta on creep–fatigue interaction behavior of reduced activation ferritic–martensitic (RAFM) steels," Fusion Engineering and Design, **100**, pp. 314–320.
[49] Schaefer, L. and Schirra, M., 1999, "Influence of thermal aging on tensile and impact bending properties of the steel grades OPTIFER and F82H mod," Journal of nuclear materials, **271**, pp. 455–458.
[50] Hasegawa, T., Tomita, Y., and Kohyama, A., 1998, "Influence of tantalum and nitrogen contents, normalizing condition and TMCP process on the mechanical properties of low-activation 9Cr–2W–0.2 V–Ta steels for fusion application," Journal of nuclear materials, **258**, pp. 1153–1157.
[51] Shiba, K., Hishinuma, A., Tohyama, A., and Masamura, K., 1997, "Properties of low activation ferritic steel F82H IEA heat. Interim report of IEA round-robin tests. 1," Japan Atomic Energy Research Institution.
[52] Tan, L., Snead, L. L., and Katoh, Y., 2016, "Development of new generation reduced activation ferritic-martensitic steels for advanced fusion reactors," Journal of Nuclear Materials, **478**, pp. 42–49.
[53] Gieseke, B., Brinkman, C., and Maziasz, P., 1992, "The influence of thermal aging on the microstructure and fatigue properties of modified 9Cr-1Mo steel," Oak Ridge National Lab., TN (United States).
[54] Cerri, E., Evangelista, E., Spigarelli, S., and Bianchi, P., 1998, "Evolution of microstructure in a modified 9Cr–1Mo steel during short term creep," Materials Science and Engineering: A, **245**(2), pp. 285–292.
[55] Shrestha, T., Basirat, M., Charit, I., Potirniche, G. P., Rink, K. K., and Sahaym, U., 2012, "Creep deformation mechanisms in modified 9Cr–1Mo steel," Journal of Nuclear Materials, **423**(1-3), pp. 110–119.
[56] Dimmler, G., Weinert, P., Kozeschnik, E., and Cerjak, H., 2003, "Quantification of the Laves phase in advanced 9–12% Cr steels using a standard SEM," Materials characterization, **51**(5), pp. 341–352.
[57] Rojas, D., Garcia, J., Prat, O., Sauthoff, G., and Kaysser-Pyzalla, A., 2011, "9% Cr heat resistant steels: Alloy design, microstructure evolution and creep response at 650 C," Materials Science and Engineering: A, **528**(15), pp. 5164–5176.
[58] Liu, Z., Huo, X., Yu, Y., Zhang, C., Xiao, N., Zhao, J., and Yang, Z., 2021, "Influence of austenitizing temperature on the mechanical properties and microstructure of reduced activation ferritic/martensitic steel," Materials Science and Engineering: A, **826**, p. 141934.
[59] Ravikirana, Mythili, R., Raju, S., Saroja, S., Jayakumar, T., and Rajendrakumar, E., 2013, "Influence of W and Ta content on microstructural characteristics in heat treated 9Cr-reduced activation ferritic/martensitic steels," Materials Characterization, **84**, pp. 196–204.
[60] Huang, Q., Baluc, N., Dai, Y., Jitsukawa, S., Kimura, A., Konys, J., Kurtz, R., Lindau, R., Muroga, T., Odette, G., Raj, B., Stoller, R., Tan, L., Tanigawa, H., Tavassoli, A.-A., Yamamoto, T., Wan, F., and Wu, Y., 2013, "Recent progress of R&D activities on reduced activation ferritic/martensitic steels," Journal of Nuclear Materials, **442**(1, Supplement 1), pp. S2–S8, FIFTEENTH INTERNATIONAL CONFERENCE ON FUSION REACTOR MATERIALS.
[61] Laliberte, F., Li, M., Almer, J., and Liu, L., 2018, "In-situ synchrotron X-ray study of microstructural evolution during creep deformation in Grade 91 steel," Materials Science and Engineering: A, **737**, pp. 115–123.
[62] Herring, C., 1950, "Diffusional viscosity of a polycrystalline solid," Journal of applied physics, **21**(5), pp. 437–445.
[63] Coble, R., 1963, "A model for boundary diffusion controlled creep in polycrystalline materials," Journal of applied physics, **34**(6), pp. 1679–1682.
[64] Kloc, L. and Sklenička, V., 1997, "Transition from power-law to viscous creep behaviour of p-91 type heat-resistant steel," Materials Science and Engineering: A, **234**, pp. 962–965.
[65] Haney, E. M., Dalle, F., Sauzay, M., Vincent, L., Tournié, I., Allais, L., and Fournier, B., 2009, "Macroscopic results of long-term creep on a modified 9Cr–1Mo steel (T91)," Materials Science and Engineering: A, **510**, pp. 99–103.
[66] Kimura, K., Sawada, K., and Kushima, H., 2014, "Creep Deformation Analysis of Grade 91 Steels and Prediction of Creep Strength Properties," *ASME 2014 Pressure Vessels and Piping Conference*, American Society of Mechanical Engineers, pp. V06AT06A039–V06AT06A039, accessed 2016-01-27, http://proceedings.asmedigitalcollection.asme.org/pdfaccess.ashx?ResourceID=7978015&PDFSource=13
[67] Argon, A., 1983, "Mechanisms and mechanics of fracture in creeping alloys," Pineridge Press, Recent Advances in Creep and Fatigue of Engineering Materials and Structures,, pp. 1–52.
[68] Dyson, B., 1983, "Continuous cavity nucleation and creep fracture," Scr. Metall.;(United States), **17**(1).
[69] Panait, C. G., Zielińska-Lipiec, A., Koziel, T., Czyrska-Filemonowicz, A., Gourgues-Lorenzon, A.-F., and Bendick, W., 2010, "Evolution of dislocation density, size of subgrains and MX-type precipitates in a P91 steel during creep and during thermal ageing at 600°C for more than 100,000h," Materials Science and Engineering: A, **527**(16), pp. 4062–4069.
[70] Sket, F., Dzieciol, K., Borbély, A., Kaysser-Pyzalla, A. R., Maile, K., and Scheck, R., 2010, "Microtomographic investigation of damage in E911 steel

after long term creep," Materials Science and Engineering: A, **528**(1), pp. 103–111.
[71] Choudhary, B. and Samuel, E. I., 2011, "Creep behaviour of modified 9Cr–1Mo ferritic steel," Journal of nuclear materials, **412**(1), pp. 82–89.
[72] Rovinelli, A., Messner, M., and Sham, T.-L., 2020, "Initial microstructural model for creep-fatigue damage in Grade 91 steel," Argonne National Lab.(ANL), Argonne, IL (United States).
[73] Pérez-Foguet, A., Rodríguez-Ferran, A., and Huerta, A., 2001, "Consistent tangent matrices for substepping schemes," Computer methods in applied mechanics and engineering, **190**(35-36), pp. 4627–4647.
[74] Quey, R., Dawson, P. R., and Barbe, F., 2011, "Large-scale 3D random polycrystals for the finite element method: Generation, meshing and remeshing," Computer Methods in Applied Mechanics and Engineering, **200**(17-20), pp. 1729–1745.
[75] Nguyen, V. P., 2014, "An open source program to generate zero-thickness cohesive interface elements," Advances in Engineering Software, **74**, pp. 27–39.
[76] Messner, M., Truster, T., Cochran, K., Parks, D., and Sham, T.-L., 2017, "Fy17 status report on the micromechanical finite element modeling of creep fracture of grade 91 steel," Argonne National Lab.(ANL), Argonne, IL (United States).
[77] Sakane, M. and Hosokawa, T., 2001, "Biaxial and triaxial creep testing of type 304 stainless steel at 923 k," *IUTAM Symposium on Creep in Structures: Proceedings of the IUTAM Symposium held in Nagoya, Japan, 3–7 April 2000*, Springer, pp. 411–418.
[78] Messner, M. C., Nassif, O., Ma, R., Truster, T. J., Cochran, K., Parks, D., and Sham, T., 2019, "Combined crystal plasticity and grain boundary modeling of creep in ferritic-martensitic steels: II. The effect of stress and temperature on engineering and microstructural properties," Modelling and Simulation in Materials Science and Engineering, **27**(7), p. 075010.
[79] Tuo, R. and Wu, C. F. J., 2015, "Efficient calibration for imperfect computer models," The Annals of Statistics, **43**(6), pp. 2331 – 2352.
[80] Hyman, J. M., 1983, "Accurate monotonicity preserving cubic interpolation," SIAM Journal on Scientific and Statistical Computing, **4**(4), pp. 645–654.
[81] Eubank, R. L., 1988, *Spline smoothing and nonparametric regression*, Marcel Dekker.
[82] Jones, D. R., Schonlau, M., and Welch, W. J., 1998, "Efficient global optimization of expensive black-box functions," Journal of Global optimization, **13**, pp. 455–492.
[83] Santner, T. J., Williams, B. J., Notz, W. I., and Williams, B. J., 2003, *The design and analysis of computer experiments*, Vol. 1, Springer.
[84] Rasmussen, C. E. and Williams, C. K. I., 2006, *Gaussian processes for machine learning*, Vol. 1, Springer.
[85] Joseph, V. R., Gul, E., and Ba, S., 2015, "Maximum projection designs for computer experiments," Biometrika, **102**(2), pp. 371–380.
[86] Joseph, V. R., Gul, E., and Ba, S., 2020, "Designing computer experiments with multiple types of factors: The MaxPro approach," Journal of Quality Technology, **52**(4), pp. 343–354.
[87] McKay, M. D., Beckman, R. J., and Conover, W. J., 1979, "A Comparison of Three Methods for Selecting Values of Input Variables in the Analysis of Output from a Computer Code," Technometrics, **21**(2), pp. 239–245.
[88] Johnson, M. E., Moore, L. M., and Ylvisaker, D., 1990, "Minimax and maximin distance designs," Journal of statistical planning and inference, **26**(2), pp. 131–148.
[89] Bonilla, E. V., Chai, K., and Williams, C., 2007, "Multi-task Gaussian process prediction," Advances in neural information processing systems, **20**.
[90] Alvarez, M. A., Rosasco, L., Lawrence, N. D., et al., 2012, "Kernels for vector-valued functions: A review," Foundations and Trends® in Machine Learning, **4**(3), pp. 195–266.
[91] Ramsay, J. and Silverman, B., 2006, *Functional Data Analysis*, Springer Series in Statistics, Springer New York.
[92] Jolliffe, I. T. and Cadima, J., 2016, "Principal component analysis: a review and recent developments," Philosophical transactions of the royal society A: Mathematical, Physical and Engineering Sciences, **374**(2065), p. 20150202.
[93] Golub, G. H. and Welsch, J. H., 1969, "Calculation of Gauss quadrature rules," Mathematics of computation, **23**(106), pp. 221–230.
[94] Basudhar, A., Dribusch, C., Lacaze, S., and Missoum, S., 2012, "Constrained efficient global optimization with support vector machines," Structural and Multidisciplinary Optimization, **46**, pp. 201–221.
[95] Hickman, R. J., Aldeghi, M., Häse, F., and Aspuru-Guzik, A., 2022, "Bayesian optimization with known experimental and design constraints for chemistry applications," Digital Discovery, **1**(5), pp. 732–744.
[96] Gelbart, M. A., Snoek, J., and Adams, R. P., 2014, "Bayesian Optimization with Unknown Constraints," 1403.5607, https://arxiv.org/abs/1403.5607
[97] Ginsbourger, D., Le Riche, R., and Carraro, L., 2010, "Kriging is well-suited to parallelize optimization," *Computational intelligence in expensive optimization problems*, Springer, pp. 131–162.
[98] Loeppky, J. L., Sacks, J., and Welch, W. J., 2009, "Choosing the sample size of a computer experiment: A practical guide," Technometrics, **51**(4), pp. 366–376.
[99] Ba, S. and Joseph, V. R., 2018, *MaxPro: Maximum Projection Designs*, R package version 4.1-2, https://CRAN.R-project.org/package=MaxPro
[100] Ramsay, J. O., Graves, S., and Hooker, G., 2020, *fda: Functional Data Analysis*, R package version 5.1.9, https://CRAN.R-project.org/package=fda
[101] Dancik, G. M. and Dorman, K. S., 2008, "mlegp: statistical analysis for computer models of biological systems using R," Bioinformatics, **24**(17), p. 1966.
[102] Kennedy, M. C. and O'Hagan, A., 2001, "Bayesian calibration of computer models," Journal of the Royal Statistical Society: Series B (Statistical Methodology), **63**(3), pp. 425–464.
[103] Nguyen, T., Luscher, D. J., and Wilkerson, J. W., 2017, "A dislocation-based crystal plasticity framework for dynamic ductile failure of single crystals," Journal of the Mechanics and Physics of Solids, **108**, pp. 1–29.
[104] Venkataraman, A. and Messner, M., 2021, "An initial framework for the rapid qualification of long-term creep rupture strength via microstructural modeling," Argonne National Lab.(ANL), Argonne, IL (United States), doi: 10.2172/1814829.
[105] Generale, A. P., Hall, R. B., Brockman, R. A., Joseph, V. R., Jefferson, G., Zawada, L., Pierce, J., and Kalidindi, S. R., 2022, "Bayesian calibration of continuum damage model parameters for an oxide-oxide ceramic matrix composite using inhomogeneous experimental data," Mechanics of Materials, **175**, p. 104487.
[106] Higdon, D., Gattiker, J., Williams, B., and Rightley, M., 2008, "Computer model calibration using high-dimensional output," Journal of the American Statistical Association, **103**(482), pp. 570–583.
[107] Sürer, Ö., Plumlee, M., and Wild, S. M., 2024, "Sequential Bayesian experimental design for calibration of expensive simulation models," Technometrics, **66**(2), pp. 157–171.
[108] Joseph, V. R. and Melkote, S. N., 2009, "Statistical Adjustments to Engineering Models," Journal of Quality Technology, **41**(4), pp. 362–375.
[109] Versino, D., Tonda, A., and Bronkhorst, C. A., 2017, "Data driven modeling of plastic deformation," Computer Methods in Applied Mechanics and Engineering, **318**, pp. 981–1004.
[110] Leyda, W. E. and Rowe, J. P., 1969, "A Study of the Time for Departure from Secondary Creep of Eighteen Steels," American Society for Metals, Tech. Rep. P 9-6.1.
[111] Raj, R. and Ashby, M., 1971, "On grain boundary sliding and diffusional creep," Metallurgical transactions, **2**, pp. 1113–1127.